

Effects of approach flow conditions on the unsteady three-dimensional wake structure of a square-back Ahmed body

Nam Kang,¹ Ebenezer E. Essel^{1,2}, Vesselina Roussinova^{1,2}, and Ram Balachandar^{1,2,*}

¹*Department of Mechanical, Automotive and Materials Engineering, University of Windsor, Windsor, Ontario, Canada N9B 3P4*

²*Department of Civil and Environmental Engineering, University of Windsor, Windsor, Ontario, Canada N9B 3P4*



(Received 14 December 2020; accepted 8 March 2021; published 26 March 2021)

This paper investigates the effects of approach flow conditions on the unsteady three-dimensional wake characteristics of a square-back Ahmed body using improved delayed detached eddy simulations. Two approach flow conditions were investigated: a reference uniform flow (case A) and a thick turbulent boundary layer (TBL) (case B), where the Ahmed body is fully submerged in the TBL, $\delta > H$, where δ is the boundary layer thickness and H is the total height of the body from the ground. Case A is studied extensively in the literature, whereas case B is less studied. The present results showed that the wake structure of case B is significantly different from that of case A. In particular, the wake of case A is dominated by a strong downwash flow from the top surface, but case B exhibits a much stronger upwash flow, which is induced by lower momentum of the fluid that emanates from the ground clearance and the pressure imbalance generated behind the body. For case A, conditional averaging of the flow field based on the sign of the drift force demonstrated the occurrence of the well-known wake switching (bimodality) event in the spanwise direction. However, the bimodality was completely suppressed in the wake of the Ahmed body submerged in the TBL. Both time-averaged turbulence statistics such as the Reynolds stresses and production terms, and time-resolved statistics including spectral analysis and temporal cross correlations are used to explore the differences between the wake structure of the Ahmed body in a uniform flow and thick TBL.

DOI: [10.1103/PhysRevFluids.6.034613](https://doi.org/10.1103/PhysRevFluids.6.034613)

I. INTRODUCTION

Turbulent flow past a blunt bluff body is of particular interest for the aerodynamic drag reduction of commercial vehicles caused by the flow separation, which leads to the formation of a low-pressure recirculation region on the rear end. The aerodynamic drag on the vehicles can lead to high fuel consumption, especially in highway driving conditions. For example, the aerodynamic drag on buses and truck trailers accounts for about 30%–70% of fuel consumption [1], which contributes substantially to greenhouse gas (GHG) emissions. With increasing global interest on strategies to mitigate GHG emissions and the alarming effects of climate change on ecosystems, economies, and communities, the transportation industry is critically evaluating methods to reduce aerodynamic drag and fuel consumption of commercial vehicles such as buses and truck trailers. One emergent avenue is the electrification of the transportation industry; however, the performance and driving range of fully electric and hybrid vehicles also depend on the aerodynamic drag. Therefore it is

*rambala@uwindsor.ca

TABLE I. Summary of pertinent recent studies on the turbulent flow characteristics around simplified square-back vehicle models. (PIV: particle image velocimetry, TPIV: tomographic PIV, LDV: laser Doppler velocimetry, LES: large eddy simulation, IDDES: improved delayed detached eddy simulation; L_r : length of the recirculation region behind the Ahmed body is demonstrated in Fig. 6.)

Author	Model	Case	Technique	10^{-4}Re_h	δ/H	C/h	L_r/h
Grandemange <i>et al.</i> [4]	Ahmed body	A	PIV	9.2	0.074	0.17	1.47
Grandemange <i>et al.</i> [8]	Ahmed body	A	PIV	3.3	0–0.06	–0.74	1.17–1.97
Evrard <i>et al.</i> [9]	Ahmed body	A	PIV	40.0	–	0.11	1.50
Volpe <i>et al.</i> [67]	Ahmed body	A	PIV	77.0	0.070	0.17	1.50
McArthur <i>et al.</i> [5]	Lorry model	A	PIV	3.8	0.090	0.14	0.90
Barros <i>et al.</i> [11]	Ahmed body	A	PIV	20.0	0.029	0.16	1.50
Lucas <i>et al.</i> [12]	Ahmed body	A	LES	40.1	0.046	0.10	1.41
Rodriguez <i>et al.</i> [13]	Ahmed body	A	LDV	5.0	–	0.28	1.39
Bonnivion and Cadot [14]	Ahmed body	A	PIV	40.0	–	0.11	1.50
Dalla Longa <i>et al.</i> [3]	Ahmed body	A	LES	3.3 and 2.0	–	0.17 and 0.59	1.45 and 1.17
	and Lorry model						
Fan <i>et al.</i> [15]	Ahmed body	A	PIV and IDDES	9.2	0.054	0.17	1.43 and 1.49
Pavia <i>et al.</i> [6]	Windsor body	A	TPIV	57.8	–	0.17	1.45
Plumejeau <i>et al.</i> [16]	Ahmed body	A	PIV	42.9	–	0.10	1.41
Podvin <i>et al.</i> [17]	Ahmed body	A	LES	1.0	–	0.13	–
Haffner <i>et al.</i> [10]	Ahmed body	A	PIV	50.0	0.028	0.17	1.58
Essel <i>et al.</i> [18]	Ahmed body	B	PIV	1.7	1.75	0.33	1.36
Present study	Ahmed body	A and B	IDDES	1.4 and 1.7	0.090 and 1.75	0.33	1.44

essential to conduct comprehensive investigations to improve our physical understanding of the turbulent flow past blunt bluff bodies that mimic road vehicles.

In the past, several experimental and numerical studies have been conducted using simplified vehicle models such as the Ahmed body, Windsor body, and the lorry model to document the salient flow features and wake characteristics behind the vehicle models [2–7]. A summary of recent pertinent articles in the literature and the geometric and initial conditions investigated are presented in Table I. The previous studies have shown that the flow around the simplified vehicle models is highly three dimensional (3D) and characterized by complex turbulent phenomena such as unsteady flow separation, vortex shedding, and flapping motion which leads to enlargement or contraction of the recirculation region behind the body. As shown in the table, most of the previous studies examined the flow characteristics around simplified vehicle models in a uniform flow or thin turbulent boundary layer (TBL) ($\delta \ll H$, where δ is the boundary layer thickness and H is the total height of the body from the ground), denoted as case A in this study. On the other hand, the wake characteristics of vehicle models in a thick TBL ($\delta \gg H$) (denoted as case B) have received less attention. For $\delta \gg H$, the vehicle model encounters stronger mean shear and larger momentum deficit near the ground which may influence the underbody flow between the base of the model and the ground and can further complicate the wake dynamics behind the model when compared to case A. Therefore this study aims at improving our understanding of the effects of the two approach flow conditions (uniform flow or thin TBL, and thick TBL) on the unsteady 3D wake characteristics of the generic square-back Ahmed body.

Figure 1 shows the dimensions and nomenclature of the square-back Ahmed body used in this study, where L , W , and h are the length, width, and height of the body, respectively. The fore end of the body has rounded edges of radius R to minimize the effects of flow separation. The clearance distance between the underbody and the ground is denoted as C . The approach flow has a boundary layer thickness of δ and a free stream velocity of U_∞ . For the uniform flow or thin TBL case

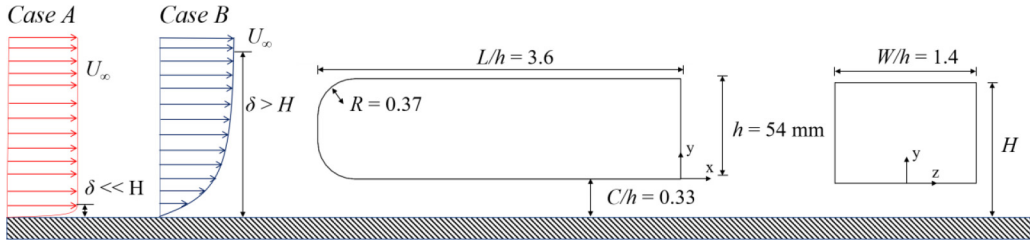


FIG. 1. Schematic drawing of the Ahmed body showing the flow nomenclature and test conditions investigated. Case A: uniform approach flow or thin turbulent boundary layer (TBL), $\delta \ll H$, and case B: thick approach TBL, $\delta > H$.

(case A), $\delta \ll H$, while for the thick TBL case (case B), $\delta > H$ (see Fig. 1). The left-handed Cartesian coordinate system adopted has the origin of the streamwise (x), wall-normal (y), and spanwise (z) directions at the midpoint of the lower edge of the back end of the body.

The wake characteristics behind the square-back Ahmed body are largely influenced by the ground clearance ratio (C/h or C/W as defined by Grandemange *et al.* [8]) and the inclusion of wheels [3,8,16]. According to Grandemange *et al.* [8], the effect of the ground on the underbody flow and the wake behind the body can be categorized into three main regimes: low ground clearance ($C/h < 0.07$), moderate ground clearance ($C/h \in [0.07, 0.12]$) and high ground clearance ($C/h > 0.12$). For low ground clearance, the momentum of the underbody flow is significantly damped by the viscous effects on the ground, leading to the formation of a single recirculation bubble behind the body. As the ground clearance increases to a moderate regime, the viscous effects gradually decrease while the momentum of the underbody flow increases such that the underbody flow exits the clearance as a jetlike upwash flow behind the body. The upwash flow interacts with the downwash flow from the top surface to form a pair of recirculation bubbles behind the body. Moreover, the upwash flow also separates on the ground due to a severe adverse pressure gradient (APG) which may generate a third recirculation bubble attached to the ground and downstream of the pair behind the body. In the case of high ground clearance, the underbody flow is more energetic and transitions to a strong upwash flow that suppresses flow separation on the ground. As a result, only a pair of recirculation bubbles are formed behind the body, manifesting the presence of the toroidal structure observed in previous studies [12,19]. Gulyás *et al.* [20] and Pavia *et al.* [6] investigated the effects of the wheels on the wake characteristics and found that the inclusion of the wheels enhanced the upwash of the underbody flow into the wake, which in turn increased the drag.

An interesting feature of the 3D bluff bodies is the phenomenon of bimodal instability where the wake flips between two asymmetric or symmetry-breaking states. This phenomenon was first recognized by Herry *et al.* [21] downstream of a 3D backward-facing step (BFS) and since then several studies have observed the bimodal behavior on other 3D bluff bodies including the Ahmed body [4,16,22–26]. However, the dynamics of the bimodal instability is influenced by perturbations due to various passive flow control parameters such as ground clearance ratio [8,16], aspect ratio [3,8], yaw and pitch angles [10,14], control cylinders and meshes [11,27], and rear end body cavity [9,12]. Active flow control strategies with the use of pulsed jets and oscillating side flaps have also been used to alter the bimodality of the wake of 3D bluff bodies [22,24,28–30]. Grandemange *et al.* [8] investigated bimodal behavior behind a square-back Ahmed body and found that the behavior depends on the ground clearance ratio and the aspect ratio (W/h) of the body. In particular, the bimodality behavior was persistent for moderate and high ground clearance, $C/h \geq 0.07$, but suppressed for low ground clearance. For aspect ratio, $W/h > 1$, the symmetry breaking occurs in the spanwise direction in the wake while for $W/h < 1$, the symmetry-breaking occurs in the wall-normal direction [3,8]. Previous studies have also shown that the bimodality is suppressed with the introduction of a yaw or pitch angle [10,14].

Most of the previous studies on the unsteady wake characteristics and the bimodality behavior around an Ahmed body were conducted experimentally with the use of time-resolved particle image velocimetry (TR PIV) [4,8–11,15]. Numerical studies, on the other hand, are limited due to the high computational cost associated with simulations at high Reynolds number and the large timescale required to capture the bimodality behavior. Nonetheless, unsteady simulations of the flow around an Ahmed body have been conducted with large eddy simulations (LES) [3,12], partially averaged Navier-Stokes (PANS) [31], unsteady Reynolds-averaged Navier-Stokes simulations (URANS) [32], and detached eddy simulations (DES) [33]. Lucas *et al.* [12], for example, captured the asymmetry of the wake using LES simulation, but the wake switching event could not be captured due to computational limitations. Using LES simulations, Dalla Longa *et al.* [3] and Podvin *et al.* [17] successfully captured the two asymmetric states of the wake at $\text{Re}_h = 3.3 \times 10^4$ and 1×10^4 , respectively. DES simulations have also been shown to have good agreement with experimental results [33,34]; however, the bimodality of the wake was not investigated in these studies.

While the aforementioned studies have greatly improved our understanding of the wake characteristics of the square-back Ahmed body, these studies were all conducted with uniform or thin approach TBL (see Table I); therefore the influence of the thick approach TBL on the wake flow around the body is not well understood. Recently, Essel *et al.* [18] conducted a study to investigate the effects of slant angle on the wake characteristics between two tandem (in-line) Ahmed bodies fully immersed in a thick TBL ($\delta/H > 1$). The slant angle of the leading body in the tandem arrangement was varied from a square back ($\alpha = 0^\circ$) to $\alpha = 35^\circ$. The experiments were conducted with planar PIV measurements in the wall-normal symmetry ($x-y$) plane of the tandem Ahmed bodies and a reference single square-back Ahmed body. The boundary layer thickness of the approach flow was $\delta/H = 1.75$ and the Reynolds number, $\text{Re}_h = U_\infty h/v = 1.7 \times 10^4$, where $v = 10^{-6} \text{ m}^2/\text{s}$ is the kinematic viscosity of water at room temperature. The Ahmed bodies had a high clearance ratio of $C/h = 0.33$ from the ground. The study examined the time-averaged turbulence statistics including the mean velocities, Reynolds stresses, and the production of turbulent kinetic energy in the $x-y$ plane. The results showed that the tandem bodies with a square-back leading model exhibited a much stronger upwash flow than downwash flow in the intervehicular spacing between the bodies. This enhanced upwash flow was also observed behind the single square-back Ahmed body. In contrast, the tandem bodies with slanted rear end of the leading model showed much stronger downwash flow in the intervehicular space.

The objective of the present study is to investigate the effects of approach flow conditions on the unsteady 3D wake characteristics of a single square-back Ahmed body using improved delayed detached eddy simulations (IDDES). Two different approach flow conditions are investigated: a reference uniform flow or thin TBL (case A) and a thick TBL (case B). The inlet flow condition used for case B is similar to that used in the previous work from our research group [18]. However, the focus of this study is significantly different as the present one examines more detailed aspects of the time-averaged statistics and the unsteady 3D wake dynamics of case B in comparison to case A. Furthermore, the occurrence of bimodality under the two approach flow conditions is also investigated using spectral analysis and high-frequency evolution of 3D vortical structures behind the Ahmed body.

II. NUMERICAL SETUP AND VALIDATION

A. Governing equations and turbulence model

The numerical simulations were performed using STAR-CCM+ computational fluid dynamics (CFD) software. STAR-CCM+ has been well used and validated in previous studies for flow past bluff bodies [15,34,35]. The flow field was simulated using transient 3D continuity and momentum equations which were solved using the finite volume method (FVM). The governing equations are discretized in time and space with the implicit second-order time and a hybrid-bounded central difference scheme [36], respectively. The system of algebraic equations resulting from the

discretization was solved using a segregated algorithm, where the continuity and momentum equations are solved sequentially [37]. These equations can be expressed in a general transport equation for a quantity φ as follows:

$$\frac{\partial}{\partial t} \int_{CV} \rho \varphi dV + \oint_A \mathbf{n} \cdot (\rho \varphi \mathbf{u}) dA = \oint_A \mathbf{n} \cdot (\Gamma_\varphi \nabla \varphi) dA + \int_{CV} S_\varphi dV, \quad (1)$$

where ρ is density, \mathbf{u} is the velocity vector, \mathbf{n} is the unit vector normal to the surface element dA in an outward direction, Γ_φ is the diffusion coefficient, and ∇_φ is the gradient operator [38]. The 3D control volume is denoted as CV while A is the surface on which the integration is performed. The first term from the left side of the equation describes the rate at which φ changes within the control volume and the second term quantifies the flux of φ through the bounding surface due to advection. The third term illustrates the rate of change of φ due to diffusive flux across the bounding surface and the last term signifies the change in φ as a result of a source term within the control volume, for example, body forces and pressure gradient.

To model the turbulent flow field, the hybrid RANS-LES approach was adopted to reduce computational cost while effectively simulating the unsteady wake characteristics around the Ahmed body. The hybrid RANS-LES approach uses a RANS-based turbulence model to simulate the boundary layer near the walls and LES for the portion of the flow field away from the walls. This hybrid approach involving RANS reduces the computational resources required for full-scale LES of engineering flows; therefore it has attracted significant interest in the research community and the industries alike. Spalart *et al.* [39] proposed the first version of the hybrid RANS-LES formulation that is well known as DES. The DES uses the local grid refinement to initiate the switch from RANS to LES, but this has resulted in several issues including log-layer mismatch. To resolve this limitation, Shur *et al.* [40] proposed the IDDES formulation that combines the capabilities of the delayed detached eddy simulation (DDES) [41] and the wall modeling in LES (WM LES). With IDDES, the model defines a new subgrid length scale that depends on both the local grid refinement and the wall-normal distance from the wall. This mitigates the log-layer mismatch problem by delaying the switch from RANS to LES near the wall. Moreover, the IDDES has been shown to surpass the DES and DDES by providing a more accurate prediction of separated and reattached flows and wake behind bluff bodies [15,33,35,42]. Therefore IDDES was used in the present study. For the RANS portion, the $k-\omega$ shear stress transport (SST) model [43] was used since the model has been shown to perform better in flows with separation and APG [38,44]. The detailed descriptions of the formulations for the SST and IDDES models are available in Menter [43] and Shur *et al.* [40], respectively, and are not repeated here for brevity.

For each simulation, the time step was set to 5×10^{-4} to ensure that the Courant number was less than 1.5 [45] and the total simulation time was 350 s. The flow statistics were collected over the last 340 s, which is equivalent to 460 vortex shedding cycles based on the Strouhal number, $St = fh/U_\infty = 0.15$ (where f is the frequency and U_∞ is the free stream velocity) calculated from the time history of the lift coefficient. The solution was considered converged when the residual of variables such as continuity, momentum, turbulent kinetic energy, and scalar dissipation rate fell below 10^{-6} .

B. Model setup and boundary conditions

The square-back Ahmed body simulated has an aspect ratio $W/h = 1.4$ and ground clearance ratio $C/h = 0.33$ (Fig. 1). The computational domain for the simulations is presented in Fig. 2. For both cases A and B, the height of the domain ($2.5h$) was set to match the water depth ($d = 0.135$ m) of the experimental work of Essel *et al.* [18], while the width of the domain was set to about $15h$ (i.e., $7.5h$ from the centerline) to minimize any potential blockage effects. The domain has a length of $26h$ with the Ahmed body positioned at about $11h$ from the inlet. This streamwise distance allowed the prescribed inlet conditions to adjust to the boundary conditions before the approach flow encounters the body. The computational mesh was constructed using an automated structured mesh generator

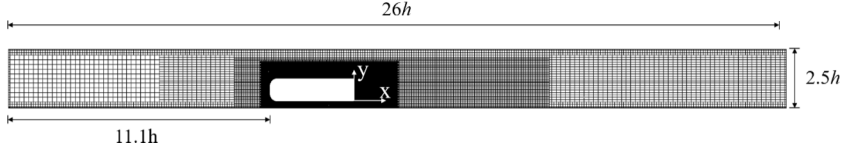


FIG. 2. Mesh configuration for both cases A and B.

to have four levels of local grid refinements as shown in Fig. 2. In terms of boundary conditions, a no-slip condition was specified on the bottom surface of the domain and the surfaces of the Ahmed body, while a free-slip condition was specified on the sides and top surface of the domain. The outlet of the domain was set as a pressure outlet. The working fluid for the simulations was set to water at room temperature (20°C) with a kinematic viscosity of $\nu = 10^{-6} \text{ m}^2/\text{s}$ to match the Reynolds number of case B with the experiments [18].

For the inlet condition, a separate 3D open channel simulation was performed to reproduce the approach flow condition of Essel *et al.* [18] and the results of the mean velocities and turbulence intensities were specified at the inlet of the domain for case B. As shown in Fig. 3, the profiles of the streamwise mean velocity and the streamwise turbulence intensity for the simulation are in good agreement with the experimental results. The boundary layer thickness for case B is $\delta/H = 1.75$; the free stream velocity and the bulk velocity are $U_{\infty} = 0.31 \text{ m/s}$ and $U_b = 0.27 \text{ m/s}$, respectively. The free stream turbulence intensity is 3.0%. Since the Ahmed body is submerged in the TBL ($\delta/H > 1$), it is important to characterize the section of the approach flow that would have stronger interaction with the body. As illustrated in the plots, the fore end of the Ahmed body is expected to encounter part of the overlap region, $y^+ \in [240, 730]$, which corresponds to $U^+ \in [18, 21]$, where $y^+ = yU_{\tau}/\nu$ and $U^+ = U/U_{\tau}$, U_{τ} is the friction velocity, and ν is the kinematic viscosity. In the outer coordinates, this section of the TBL corresponds to $y/d \in [0.1, 0.5]$ with reduced mean velocities of $0.7U_{\infty} - 0.9U_{\infty}$ and elevated turbulence intensities of 4.5% – 6.5%. For the uniform approach flow test case (case A), the Dirichlet condition was used with an inlet velocity of 0.27 m/s (based on U_b of case B) and a low turbulence level of 1.0%. The approach boundary layer thickness without the body in the flow field was $\delta/H = 0.09$ for case A. The Reynolds number based on U_b and h is $\text{Re}_b = 1.4 \times 10^4$ for each test case.

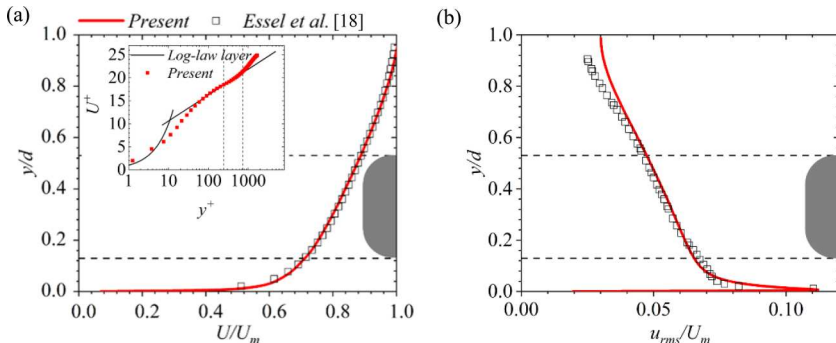


FIG. 3. Approach flow condition specified at the inlet of the simulation for case B compared with the experimental results of Essel *et al.* [18]. (a) Streamwise mean velocity profile normalized in outer coordinates (U_{∞} and d) and logarithmic form (inset), $U^+ = 1/\kappa(y^+) + B$, where the von Kármán constant $\kappa = 0.41$, and the intercept is set at $B = 5.0$, and (b) streamwise turbulence intensity profile in outer coordinate. The dashed horizontal lines in (a,b) represent the location of the bluff body in the outer coordinates, whereas the vertical solid lines in the inset of (a) represent the location of the bluff body in the inner coordinates.

TABLE II. Summary of grid properties for mesh sensitivity test.

Grid	10^{-6} Cell count	C_D	C_{pb}	L_r/h	y_{body}^+	y_{grnd}^+
I	5.0	0.30	-0.13	1.31	2.15	1.52
II	6.8	0.31	-0.14	1.44	0.42	0.68
III	13.1	0.31	-0.15	1.43	0.08	0.26

Following Castelain *et al.* [27], the underbody bulk velocity has a significant impact on the wake structure of the vehicle model. Here, the underbody bulk velocity determined near the fore end of the Ahmed body ($x/h = -0.34$) was $0.31U_\infty$ for case A and $0.19U_\infty$ (40% lower) for case B. At the rear end of the body ($x/h = 0$) the pressure losses result in a reduction of the underbody bulk velocity to $0.23U_\infty$ and $0.15U_\infty$ for cases A and B, respectively. Despite the reduced momentum flux of case B, the underbody bulk velocities obtained for both cases are within ranges of $0.10U_\infty - 0.40U_\infty$ reported for full-scale trucks [27]. This observation is attributed to the high ground clearance ratio ($C/h = 0.33$) used in the present study.

C. Mesh sensitivity and validation

Mesh sensitivity tests were carried out to ensure that the grid refinements were sufficient for accurate numerical solution without any compromise on the statistical convergence of the results. This was performed using three [coarse (grid I), medium (grid II), and fine (grid III)] different meshes with increasing number of cell counts as presented in Table II. These assessments were performed using case B since the mean shear near the bottom wall is much stronger than that of case A; therefore a mesh chosen for case B is expected to perform well for case A as well. Detailed results of the assessments are presented in Kang [46]; however, the results of C_D , C_{pb} , L_r , and y^+ for the three meshes are shown in Table II for brevity. It was found that the mean velocities, Reynolds stresses, and the flow parameters for grids II and III were in reasonable agreement while those for grid I were significantly different. For grids II and III, the $y^+ < 1$ indicates that the grid resolution was sufficient to simulate the viscous sublayer of the turbulent boundary layer on the walls. Moreover, the grid resolution in the recirculation region for grids II and III satisfied the Taylor microscale criterion of $\lambda_T/\Delta > 1$ [47], where λ_T is Taylor microscale and Δ is grid size. Based on the assessments, grid II was chosen for the simulations of cases A and B to reduce computational time when compared to that of grid III.

An extensive validation was carried out for case A using the experimental results of Rodriguez *et al.* [13] and for case B using the results of the single square-back Ahmed body reported in Essel *et al.* [18]. It is worth noting that the experiment by Rodriguez *et al.* [13] was conducted with a laser Doppler velocimetry (LDV) using a similar Ahmed body model, ground clearance ratio ($C/h = 0.28$), and a Reynolds number of $Re_h = 5.0 \times 10^4$. Figure 4 compares profiles of the streamwise mean velocity (U) and Reynolds stresses (\bar{u}^2 , \bar{v}^2 and $-\bar{u}'\bar{v}'$) for the present simulations and the previous experimental works. The profiles are extracted in the wake region and normalized by U_b and h . For case A [Figs. 4(a) and 4(b)], the results of the streamwise mean velocity and Reynolds shear stress for the simulations are in reasonable agreement with the experiment, except for the disparity in the peak values of the Reynolds shear stress at $x/h = 0.83$ and 1.02 . For case B, similar agreements between the simulation and the experiment can be observed in the profiles of the streamwise mean velocity and the Reynolds stresses. However, Fig. 4(c) shows that the momentum of the jetlike flow near the wall ($y/h < 0$) for the simulation is reduced compared to that of the experiment. Given the experimental and numerical uncertainties in the results, it was concluded that the present IDDES and the grid resolution are sufficient to produce results that reasonably describe the mean flow and turbulence statistics around the Ahmed bodies.

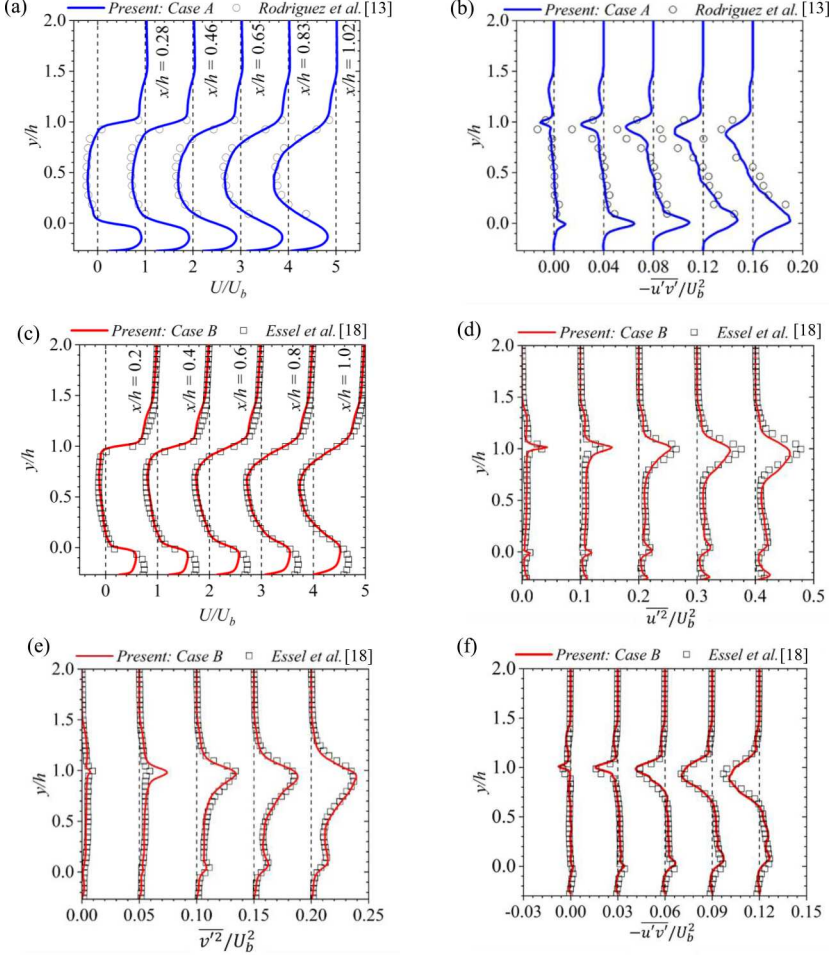


FIG. 4. Comparison between present numerical results and previous experiments for case A (Rodriguez *et al.* [13]) and case B (Essel *et al.* [18]). Case A: Profiles of (a) streamwise mean velocity U/U_b , and (b) Reynolds shear stress $-\bar{u}'\bar{v}'/\bar{U}_b^2$. Case B: Profiles of (c) streamwise mean velocity U/U_b , (d) streamwise Reynolds normal stress \bar{u}^2/\bar{U}_b^2 , (e) wall-normal Reynolds normal stress \bar{v}^2/\bar{U}_b^2 , and (f) Reynolds shear stress $-\bar{u}'\bar{v}'/\bar{U}_b^2$. The profiles of U/U_b and $-\bar{u}'\bar{v}'/\bar{U}_b^2$ for case A are offset at an interval of 1.0 and 0.04, respectively, while the profiles of U/U_b , \bar{u}^2/\bar{U}_b^2 , \bar{v}^2/\bar{U}_b^2 , and $-\bar{u}'\bar{v}'/\bar{U}_b^2$ for case B are offset at an interval of 1.0, 0.1, 0.05, and 0.03 respectively. Profiles of Rodriguez *et al.* [13] were obtained from personal communication with the authors.

III. RESULTS AND DISCUSSION

The results presented focus on the flow separation and the near-wake region of the Ahmed body with emphasis on the planes (P_1 – P_5) shown in Fig. 5. The plane P_1 is used to characterize the flow field in the x – y symmetry ($z/h = 0$) plane while P_2 is used for the x – z symmetry ($y/h = 0.5$) plane of the body. Planes, P_3 , P_4 , and P_5 are extracted in the y – z plane to document the evolution of the flow within ($x/h = 0.8$) and downstream ($x/h = 1.4$ and 2.0) of the recirculation region. The results of the time-averaged turbulence statistics over the total sampling time are discussed in Secs III A–III D while instantaneous and time-resolved statistics used to characterize the large-scale vortical structures and unsteady global modes in the wake are presented in Secs. III E and III F.

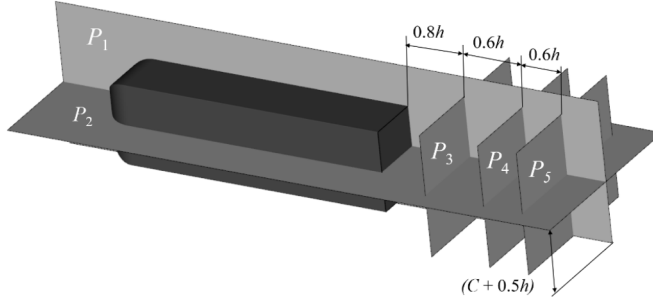


FIG. 5. Planes of interest. P_1 is the wall-normal symmetry ($z/h = 0$) plane and P_2 is the spanwise symmetry ($y/h = 0.5$) plane of the Ahmed body. The cross-sectional ($y-z$) planes are denoted as P_3 , P_4 , and P_5 with offset distances of $x/h = 0.8, 1.4$, and 2.0 , respectively, from the rear end of the body.

A. Mean flow pattern

Figure 6 shows contours of the streamwise mean velocity in the wall-normal (P_1) and spanwise (P_2) symmetry planes of the Ahmed body for both test cases. The mean streamlines are superimposed on the contours to reveal the flow pattern and the zero-contour line ($U = 0$) is used to demarcate the reverse flow regions ($U < 0$) on the body. The mean flow features are symmetric in the spanwise plane [Figs. 6(c) and 6(d)] but asymmetric in the wall-normal plane [Figs. 6(a) and 6(b)] due to the presence of the ground. Near the fore end, the separation point is fixed at the leading edge of the straight section ($x/h = -3.4$) on all four sides of the body, irrespective of the approach flow condition. As demonstrated in Fig. 6(a), the length of the recirculation region X_r/h on each side is determined as the streamwise distance from the separation point ($x/h = -3.4$) to the farthest location of the zero-contour line on the surface of the body. On the lateral sides and top surface of the body, the value of $X_r/h = 1.0$ is independent of approach flow condition. However, the length of the recirculation region increased to $X_r/h = 1.2$ on the underbody of the uniform approach flow case (case A) but decreased to $X_r/h = 0.8$ on the underbody of the thick approach TBL case (case B).

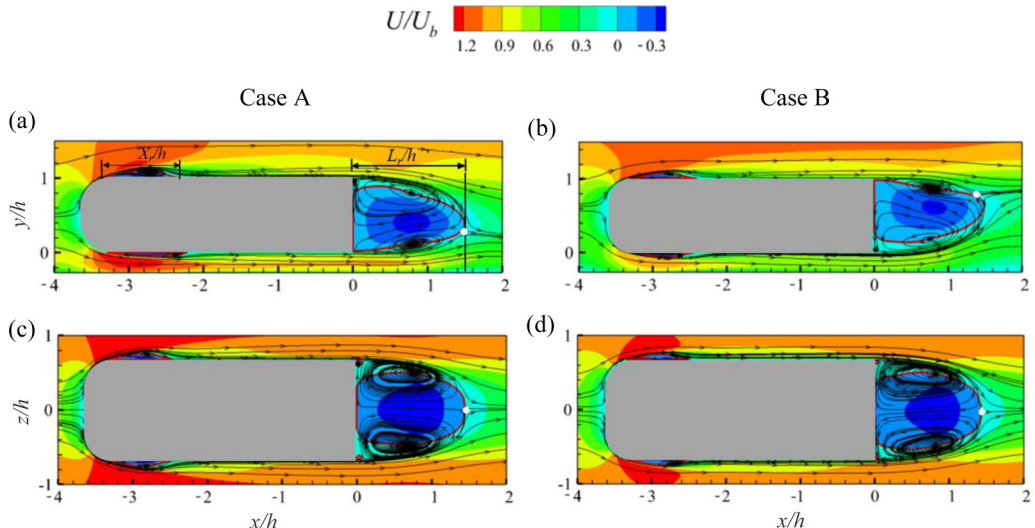


FIG. 6. Contours of the streamwise mean velocity at P_1 (a), (b) and P_2 (c), (d) for case A and case B, respectively. The red line represents the reverse flow region ($U < 0$) defined by the zero streamwise mean velocity contour line. The white dots denote the saddle points.

For case A, the magnitude of acceleration of the approach flow beneath the underbody is associated with a strong favorable pressure gradient (FPG) which suppresses the wall-normal growth of the recirculation region, thereby stretching the region in the streamwise direction. In other previous investigations on an Ahmed body in a uniform flow, the recirculation region on the underbody was found to be completely suppressed due to the effect of FPG [3,12]. For case B, the reduced length of the recirculation region on the underbody is attributed to the elevated turbulence level (6.5%) and reduced mean velocity ($0.7U_b$) of the approach flow that is accelerated beneath the body. The reduced mean velocity would lead to a milder FPG when compared with that of case A [Figs. 6(a) and 6(b)]. Moreover, high turbulence levels and reduced mean velocity in an approach flow have also been found to reduce the length of the recirculation region on bluff bodies such as blunt plates and forward-facing steps [48–50].

Behind the body, the pairs of recirculation bubbles which manifest the presence of the toroidal structure are well defined in both the wall-normal and spanwise planes for each test case. The length of the recirculation region $L_r/h = 1.44$ is independent of approach flow conditions, however; the flow topography in the wall-normal plane for the two test cases shows distinct differences due to the competing effects of the downwash flow from the top surface and the upwash jetlike flow from the underbody. The downwash flow and upwash flow meet at the saddle point indicated by the white dots. Case A exhibits the dominance of the downwash flow, which is the main source of the reverse flow that forms the pair of asymmetric recirculation bubbles. As a result, the saddle point is located closer to the ground ($y/h = 0.3$). This flow topography is consistent with the results of previous studies on square-back Ahmed bodies with a high clearance ratio $C/h > 0.12$ and in a uniform flow [8–10,16]. In contrast, case B shows an opposite behavior where the upwash flow emanating from the ground clearance is strongly deflected away from the ground, leading to the skewness of the recirculation region toward the free stream and the saddle point located at $y/h > 0.8$. This observation was found to be associated with pressure imbalance behind the body for case B, as the low-pressure region was more intense near the top rear edge of the body than near the bottom rear edge because of the reduced momentum of the underbody flow that exits the clearance. Furthermore, the results showed that the mean drag for case A ($C_D = 0.38$) decreased by about 18% in the case of case B ($C_D = 0.31$).

The wake asymmetry dynamics behind 3D bluff bodies originate from the first steady instability in the laminar regime [26,30,51] and the preferred orientation is highly sensitive to geometric and flow conditions or perturbations [8,11,14,27]. Castelain *et al.* [27] altered the wake structure behind a simplified truck model by varying the underbody bulk velocity using porous pressure reducers at a fixed approach flow condition. Barros *et al.* [11] showed that, for a fixed approach flow, a normally asymmetric wake in the wall-normal plane can transition to quasisymmetric and reversed asymmetric states with the use of small cylindrical perturbations in the underbody flow. They also found that the symmetry-breaking state in the wall-normal plane of each test case is accompanied by an inverse modification in the spanwise plane, demonstrating a symmetry exchange of the unstable wake structure. In the present study, the reversed asymmetric wake in the wall-normal plane of case B can be considered as a variant of the asymmetric wake of case A. Both test cases also demonstrate a statistically symmetric wake in the spanwise plane, in agreement with the findings by Barros *et al.* [11]. In the context of wake-altering dynamics, the present observation demonstrates a source of passive perturbation associated with ground clearance momentum deficiency, which is induced by the thick approach TBL.

Figures 7 and 8 show contours of the wall-normal and spanwise mean velocities used to examine the development of the wake structure in the cross-sectional ($x-z$) planes, $P_3 - P_5$. The plane P_3 slices through the foci of the recirculation bubbles ($x/h \approx 0.8$) while P_4 coincides with the saddle points ($x/h \approx 1.4$). As shown in Fig. 7, the spiral pattern of the streamlines for the recirculation bubbles in P_3 is well defined for case A compared to case B. This observation may manifest a distortion in the wake structure of case B caused by the strong upwash of the underbody flow. The streamlines in P_4 and P_5 demonstrate the dominance of the downwash flow in case A and the upwash flow in case B. The wall-normal mean velocity contours for case A [Figs. 8(a)–8(c)] indicate that

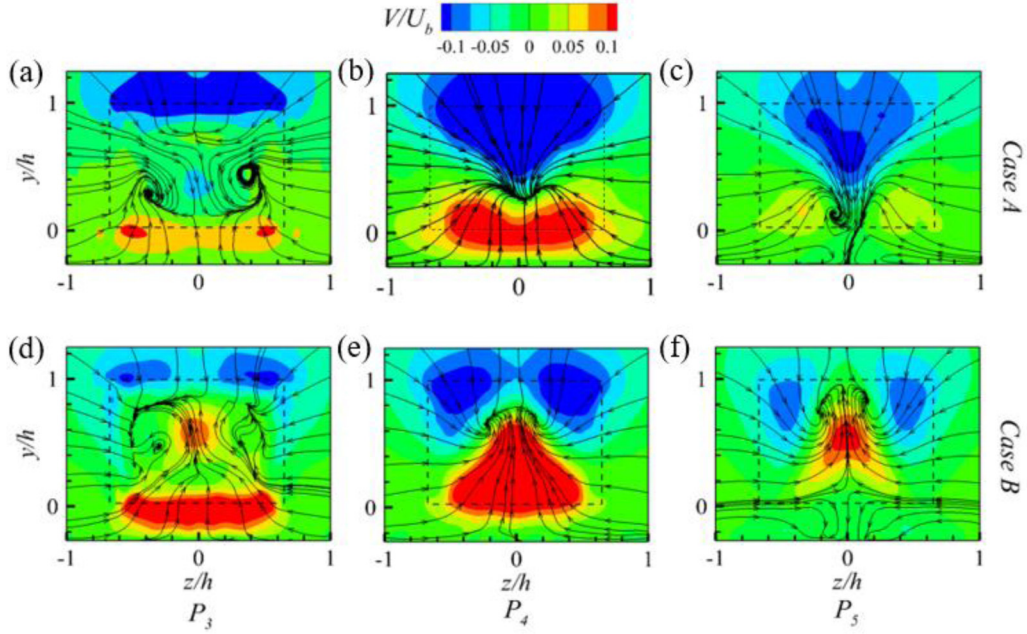


FIG. 7. Contours of wall-normal mean velocity in P_3 (a), (d), P_4 (b), (e), and P_5 (c), (f) for case A and case B, respectively. Superimposed on the contours are the mean streamlines. The dashed black lines represent the rear surface of the Ahmed body.

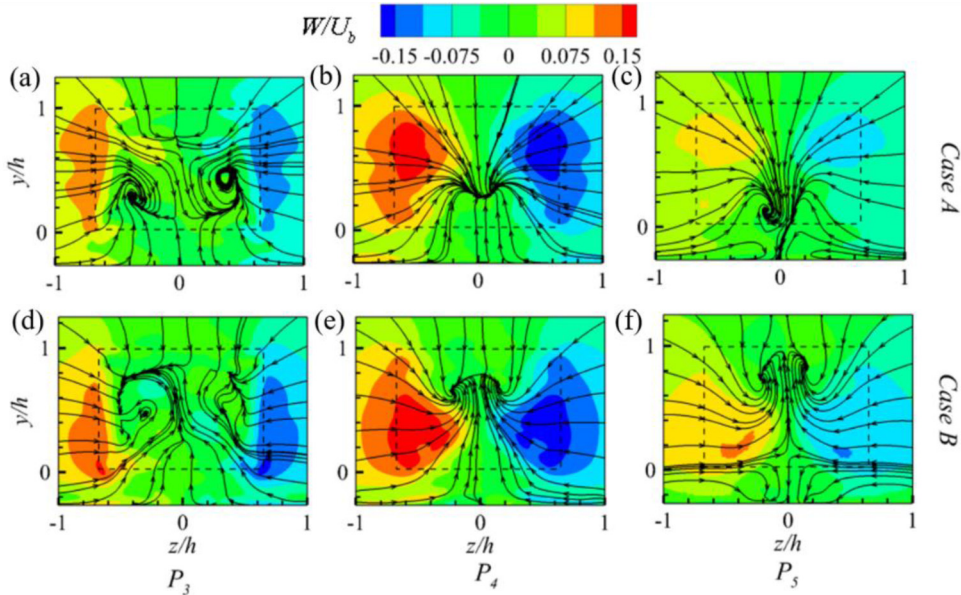


FIG. 8. Contours of spanwise mean velocity in P_3 (a), (d), P_4 (b), (e), and P_5 (c), (f) for case A and case B, respectively. Superimposed on the contours are the mean streamlines. The dashed black lines represent the rear surface of the Ahmed body.

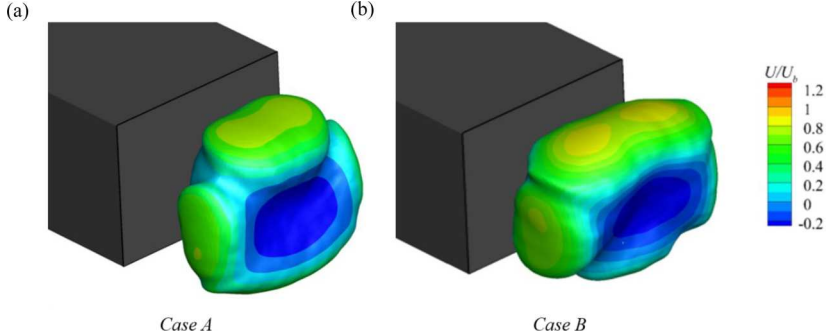


FIG. 9. Isosurfaces of mean pressure coefficient $C_p \approx -0.22$ colored by streamwise mean velocity in the wake of (a) case A and (b) case B.

the downwash flow spans the entire top edge of the body while the upwash flow spans the bottom edge in P_3 and P_4 . Further downstream, the downwash flow dominates and penetrates closer to the ground, thereby forcing the upwash flow to split up and occupy the bottom corners of the body. For case B [Figs. 7(d)–7(f)], an opposite behavior occurs where the upwash flow penetrates closer to the top edge and forces the downwash flow to split up and occupy the top corners of the body. However, the effects of the upwash flow are more severe as the split-up of the downwash flow occurs much earlier (P_4). In Fig. 8, the spanwise mean velocity contours show that the downwash flow for case A is augmented by entrainments from the lateral sides which are more intense near the top corners. As expected, an opposite entrainment behavior occurs for case B to augment the upwash flow, but unlike case A, the entrainment involves wider regions and continues to persist strongly at P_5 .

Isosurfaces of the mean pressure coefficient, $C_p = 2(p - p_o)/(\rho U_b^2)$, where p is the mean static pressure and p_o is the atmospheric pressure, are shown in Fig. 9 to reveal the toroidal structure formed behind the Ahmed body for each test case. The isosurfaces are based on a threshold value of $C_p \approx -0.22$, similar to values ($C_p \in [-0.20, -0.32]$) used in previous studies [4,12,15,19], and colored by the streamwise mean velocity. For case A, the low-pressure torus formed behind the body is akin to that observed in previous studies on Ahmed bodies in a uniform flow and without the wheels [12,19]. Case B, on the other hand, shows significant modification to the structure of the torus, especially on the upper and lower parts, when compared to that of case A. These modifications are evidence of the distortion in the wake structure caused by the stronger upwash flow in case B.

B. Growth of the downwash and upwash shear layers

The streamwise evolution of the mean flow over the top surface and underbody of the Ahmed body is examined using the distribution of the local maximum mean velocity U_m as presented in Fig. 10(a). Here, the flow over the top surface is denoted by the superscript T and the underbody flow is denoted by B . The profiles are normalized by U_∞ and h . Unlike case A, the acceleration of the approach flow to a local peak value near the fore end ($x/h \approx -3.0$) is suppressed on the top surface of case B. Beneath the underbody, the local maximum velocities for case B are consistently lower than that of case A, indicative of the reduced mean velocity in the approach flow that encounters the Ahmed body for case B. It is also interesting to notice that the U_m^B/U_∞ profiles exhibit a plateau region $x/h \in [-1.0, 0.5]$ followed by a gradual decay with streamwise distance.

For separated shear layers, the maximum velocity difference $\Delta U = U_m - U_{\min}$ [where U_{\min} is the local maximum negative (backflow) velocity in the recirculation region] is an important scaling parameter that influences the growth of the shear layers, which is defined based on the vorticity thickness $\delta_{\omega,z} = \Delta U / |\partial U / \partial y_m|$, where $|\partial U / \partial y_m|$ is the magnitude of the maximum mean shear ($\partial U / \partial y$). Most previous studies on separated shear flows such as bluff plates [52,53], BFS, and forward-facing steps (FFS) [48,54,55] have shown that the profile of the vorticity thickness exhibits

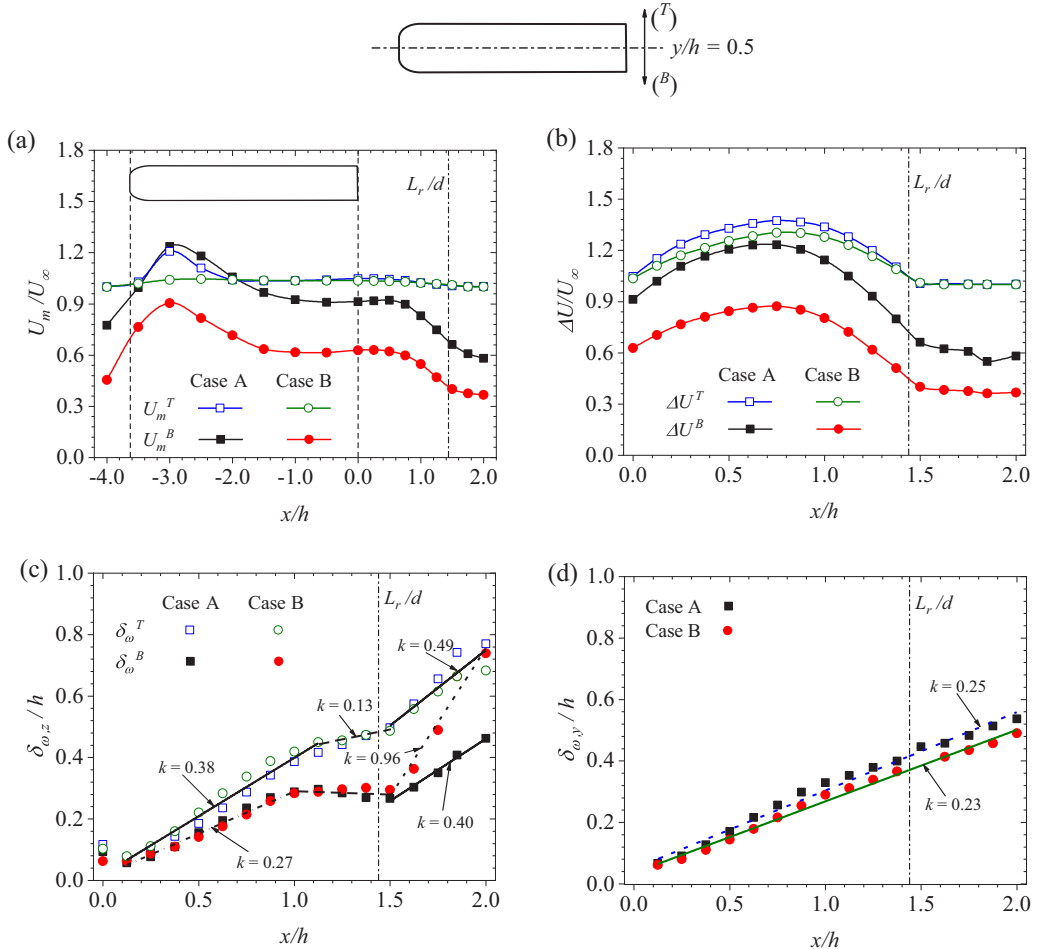


FIG. 10. Distributions of (a) local maximum mean velocity U_m/U_∞ , (b) velocity difference $\Delta U/U_\infty$, and vorticity thickness (c) $\delta_{\omega,z}/h$, and (d) $\delta_{\omega,y}/h$.

a linear growth section with a slope $k = d\delta_{\omega}/dx$ that represents the growth rate of the separated shear layer.

In this study, a similar analysis of the vorticity thickness is performed to characterize the effects of the approach flow on the separated shear layers that constitute the downwash and upwash flows in the wake region. Figures 10(b) and 10(c) present the distributions of $\Delta U/U_\infty$ and $\delta_{\omega,z}/h$, respectively, in plane P_1 . It should be noted that the maximum velocity difference in the upper shear layer ($y/h \geq 0.5$), $\Delta U^T = U_m^T - U_{\min}$, and the corresponding vorticity thickness δ_{ω}^T are associated with the downwash flow while $\Delta U^B = U_m^B - U_{\min}$ and δ_{ω}^B in the lower shear layer ($y/h \leq 0.5$) are associated with the upwash flow. The values of $\partial U/\partial y_m$ were carefully determined in each separated shear layer to avoid any bias that may arise from the elevated mean shear on the ground. For comparison, the vorticity thickness of the lateral free shear layers, $\delta_{\omega,y} = \Delta U/|\partial U/\partial z_m|$, evaluated in the plane P_2 for each test case is presented in Fig. 10(d). In Fig. 10(b), the profiles of $\Delta U^T/U_\infty$ for the downwash flow are less sensitive to the approach flow condition throughout the near-wake region, but the profiles for the upwash flow ($\Delta U^B/U_\infty$) show significant differences between cases A and B, in agreement with the U_m/U_∞ profiles [see Fig. 10(a)]. Figure 10(c) indicates that the

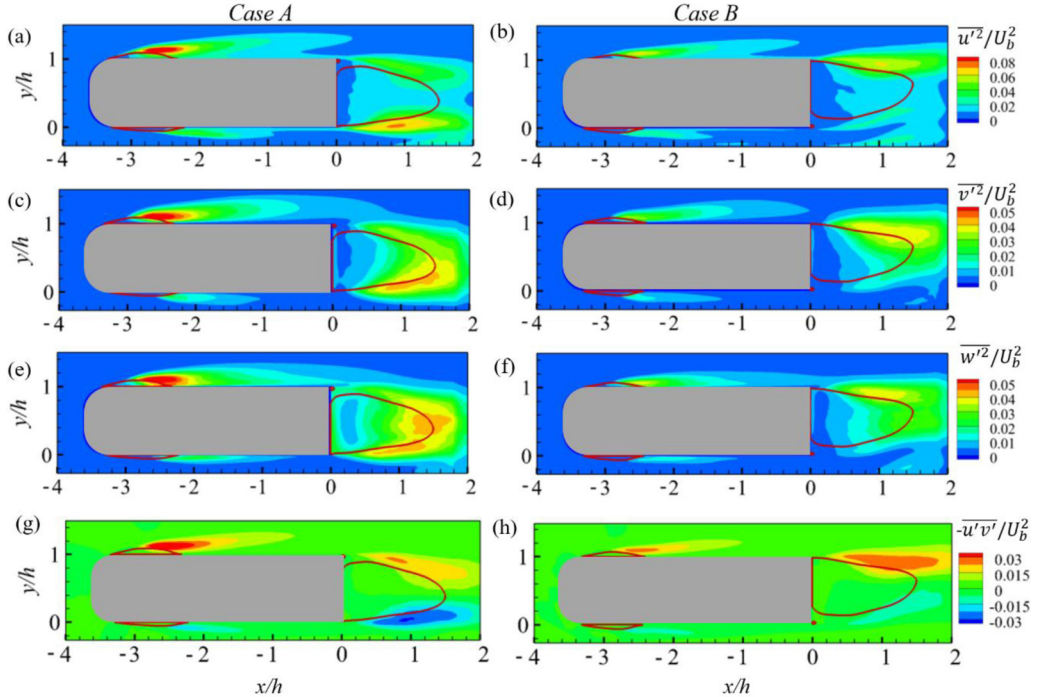


FIG. 11. Contours of Reynolds stresses in P_1 . Streamwise Reynolds normal stress $\overline{u'^2}/U_b^2$ (a), (b), wall-normal Reynolds normal stress, $\overline{v'^2}/U_b^2$ (c), (d), spanwise Reynolds normal stress $\overline{w'^2}/U_b^2$ (e), (f), and Reynolds shear stress $-\overline{u'v'}/U_b^2$ (e), (f), for case A and case B, respectively. The red line represents the reverse flow region ($U < 0$) defined by the zero streamwise mean velocity contour line.

separated shear layers for both cases grow rapidly in a similar linear fashion over the first part ($x/h \in [0.1, 1.1]$) of the recirculation region. Here, the growth rate $k = 0.38$ in the downwash flow is about 40% larger than the growth rate in the upwash flow ($k = 0.27$) for both cases. This should be expected as the growth of the downwash flow is strongly influenced by the enhanced entrainment of free stream fluid. Nonetheless, the present growth rates in the first part of the recirculation region are about 19%–60% larger than values of $k = 0.15$ – 0.22 reported for bluff plates, FFS, BFS, and plane mixing layers [53,56–58]. Agelinchaab and Tachie [59] and Fang and Tachie [54], however, reported a growth rate of $k \approx 0.30$ for separated shear layers over forward-backward facing steps. Figure 11(c) also shows that the growth rate sharply decreases in the second part of the recirculation region, similar to observations made in previous studies on separated shear flows [48,54]. The downwash flow attains a growth rate of $k = 0.13$, but the δ_ω/h values for the upwash flow are nearly constant. Beyond the recirculation region ($x/h > 1.44$), the growth rate increases rapidly due to the diminishing mean shear. It can be seen that the growth rate of the downwash flow ($k = 0.49$) is similar for both cases, but the upwash flow for case B ($k = 0.96$) grows more rapidly than that of case A ($k = 0.40$). This difference is attributed to the rapid attenuation of the mean shear in the upwash flow for case B. Unlike the downwash and upwash shear layers, the lateral free shear layers [Fig. 10(d)] grow linearly throughout the near-wake region, $x/h \in [0.1, 2.0]$. The growth rate $k = 0.24 \pm 0.01$ is independent of the approach flow condition and generally lower than the growth rates of the wall-normal shear layers. However, the growth rate of the lateral free shear layers is comparable to results of plane mixing layers and separated shear flows [53,54,56–59].

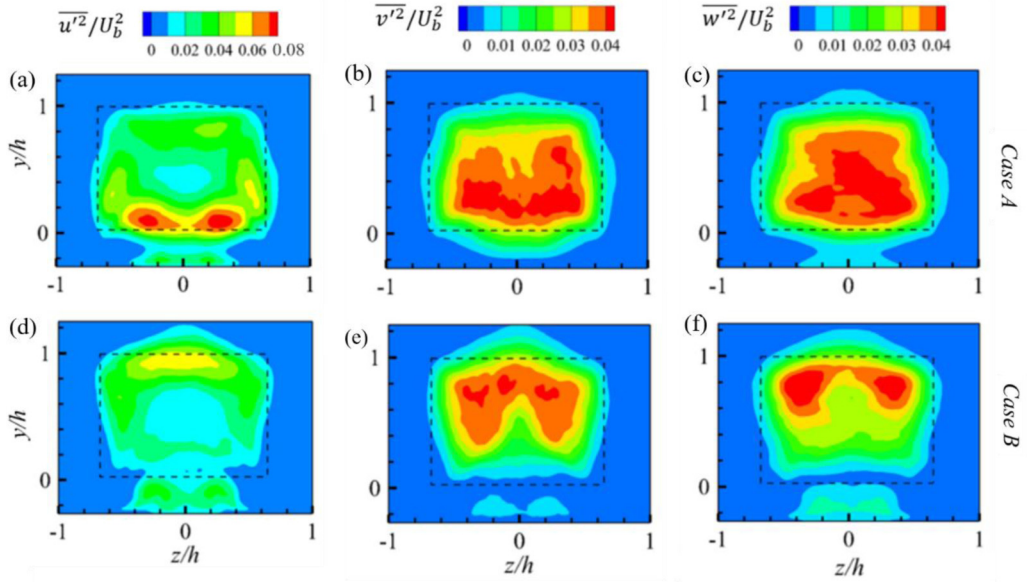


FIG. 12. Contours of Reynolds normal stresses in P_4 . Streamwise Reynolds normal stress $\overline{u'^2}/U_b^2$ (a), (d), wall-normal Reynolds normal stress $\overline{v'^2}/U_b^2$ (b), (e), and spanwise Reynolds normal stress $\overline{w'^2}/U_b^2$ (c), (f), for case A and case B, respectively. The dashed black lines represent the rear surface of the Ahmed body.

C. Reynolds stresses and anisotropy

Figure 11 presents the contours of the Reynolds normal stresses ($\overline{u'^2}$, $\overline{v'^2}$, and $\overline{w'^2}$) and the Reynolds shear stress ($-\overline{u'v'}$) in the wall-normal plane, P_1 . The corresponding Reynolds stress ($\overline{u'^2}$, $\overline{v'^2}$, $\overline{w'^2}$, and $-\overline{u'w'}$) contours in the spanwise plane P_2 exhibit reflectional symmetry with small differences in magnitude between the two test cases and, therefore, are not shown for brevity. In general, the magnitude of the Reynolds stresses for case B are reduced compared to those of case A. The Reynolds stresses exhibit strong anisotropy where the streamwise Reynolds normal stress ($\overline{u'^2}$) is the largest and the wall-normal ($\overline{v'^2}$) and spanwise ($\overline{w'^2}$) Reynolds normal stresses have similar magnitudes. In P_1 the Reynolds stresses in the separated shear layers near the fore end of the body are significantly enhanced on the top surface compared to the stresses beneath the underbody. The reduced stresses near the fore end of the underbody are attributed to the decrease in entrainment due to confinement and the damping effects of the ground. Behind the body, it is interesting to notice that the Reynolds stresses are more intense in the upwash flow for case A than that of case B, whereas the downwash flow for case B shows enhanced Reynolds stresses compared to that of case A. This observation is attributed to the asymmetric distribution of the mean shear ($\partial U/\partial y$) behind the body, which is larger in the upwash flow for case A and the downwash flow for case B.

More insights into the Reynolds stresses were obtained by examining contours in the cross-sectional planes ($P_3 - P_5$). To highlight the salient features, the contours of the Reynolds stresses in P_4 are presented in Figs. 12 and 13. The plots show that the Reynolds normal stresses [Fig. 12] are enhanced across most parts of the shear layers in the spanwise direction. For case A [Figs. 12(a)–12(c)], the streamwise Reynolds normal stress is predominant in the lower shear layer (i.e., upwash flow) while the wall-normal and spanwise Reynolds normal stresses extend into the core of the wake. Case B [Figs. 12(d)–12(f)], on the other hand, shows enhanced Reynolds normal stresses in the upper shear layer (i.e., downwash flow) and along the lateral shear layers such that the stresses are reduced in the core of the wake. This observation may be attributed to the deep penetration of

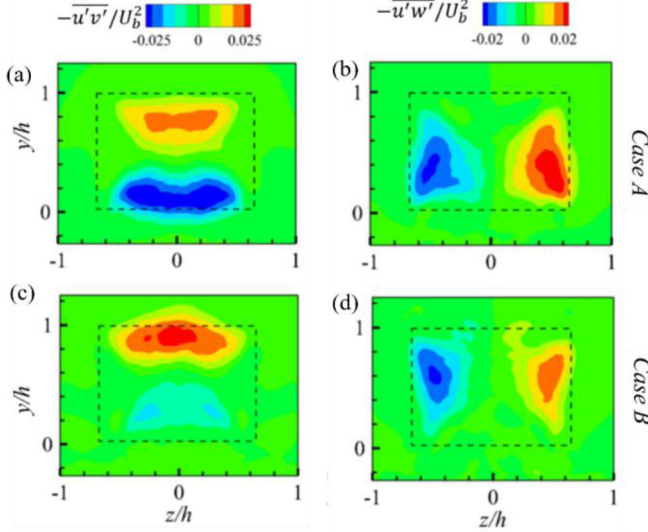


FIG. 13. Contours of Reynolds shear stresses $-\overline{u'v'}/U_b^2$ (a), (c), and $-\overline{u'w'}/U_b^2$ (b), (d), in P_4 for case A and case B, respectively. The dashed black lines represent the rear surface of the Ahmed body.

the upwash flow into the wake of case B [see Fig. 7]. In Fig. 13, $-\overline{u'v'}$ [Figs. 13(a) and 13(c)] is predominant in the upper and lower shear layers while $-\overline{u'w'}$ [Figs. 13(b) and 13(d)] is predominant in the lateral shear layers, in agreement with the orientations of $\partial U/\partial y$ and $\partial U/\partial z$, respectively. Moreover, the Reynolds shear stresses are suppressed in the lower shear layer and toward the bottom corners of the Ahmed body for case B [Figs. 13(c) and 13(d)], and the opposite behavior occurs for case A [Figs. 13(a) and 13(b)]. It should be noted that the spatial distributions of the Reynolds stresses in all the planes for case A are in good agreement with previous experimental studies on an Ahmed body in uniform flow [8,11]. As discussed earlier, the Reynolds stress contours ($\overline{u'^2}$, $\overline{v'^2}$, and $-\overline{u'v'}$) in P_1 for case B are also consistent with the experimental results in the P_1 plane of the square-back Ahmed body reported in Essel *et al.* [18].

Large-scale anisotropy is important in understanding the turbulence structure in complex turbulent flows. Here, we examine the variation of the anisotropy in the near wake of the Ahmed body in the two approach flow conditions. Specifically, the streamwise distributions of the maximum values of the Reynolds stresses were evaluated based on the normalized Reynolds stress anisotropy tensor given as

$$b_{ij} = \frac{\overline{u'_i u'_j}}{2k} - \frac{1}{3}\delta_{ij}, \quad (2)$$

where the turbulent kinetic energy $k = 0.5\overline{u_i u_i}$, δ_{ij} is the Kronecker delta, and the trace $b_{ii} \equiv 0$ is an invariant of b_{ij} . The anisotropic values of the diagonal components b_{11} , b_{22} , and b_{33} (based on the normal stresses) can lie between $-2/3$ and $4/3$, and a value of zero indicates isotropy [60].

Figures 14(a)–14(c) compare the distributions of the maximum Reynolds normal stresses in the wall-normal and spanwise symmetry planes and the corresponding anisotropic relations b_{11} , b_{22} , and b_{33} are presented in Figs. 14(d)–14(f). Figure 14(a) shows that the maximum $\overline{u'^2}$ distributions for each test case attain the highest values at about half the length of the recirculation region, followed by a gradual decrease with streamwise distance. The decay of $\overline{u'^2}$ is often associated with the breakdown of the large-scale eddies that are generated during the flow separation and roll-up of the shear layers [61,62]. The $\overline{u'^2}$ distributions are more intense in the wall-normal plane than

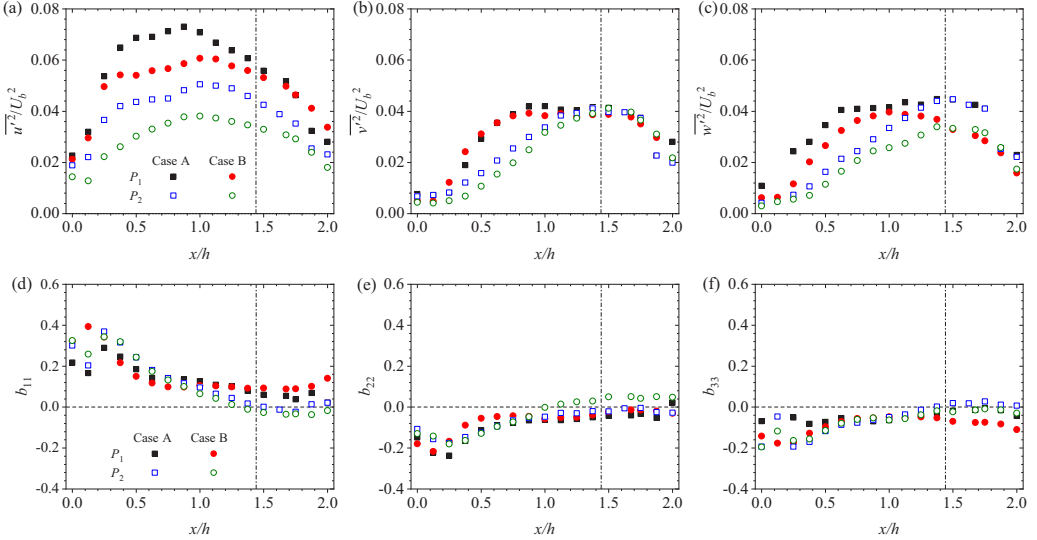


FIG. 14. Distributions of the maximum (a) streamwise, (b) wall-normal, and (c) spanwise Reynolds normal stresses and the corresponding Reynolds stress anisotropy, (d) b_{11} , (d) b_{22} , and (d) b_{33} , in the near wake of case A and case B. The vertical dashed line denotes the L_r/h .

the spanwise plane, demonstrating the dominance of the downwash and upwash flows over the lateral shear layers. The plots also show that $\overline{u'^2}$ is reduced when the Ahmed body is submerged in a TBL and the effect is more severe within the length of the recirculation region. The maximum $\overline{v'^2}$ distributions are independent of approach flow conditions; however, $\overline{w'^2}$ exhibits marginal differences between the two test cases.

As can be seen in Figs. 14(d)–14(f), strong anisotropy in the Reynolds normal stresses arises in the immediate vicinity of the body with peak values occurring at $x/h \approx 0.25$. The peak values of b_{11} are about twice the values of b_{22} and b_{33} as $b_{22} \approx b_{33}$. Further downstream, the anisotropy decreases, especially in the spanwise plane where the terms are identically zero beyond the recirculation region. In the wall-normal plane, it is observed that the anisotropy in case B tends to increase beyond the recirculation region. This is attributed to the persistence of relatively high levels of $\overline{u'^2}$ in the downwash flow of case B.

Figure 15(a) shows the distributions of the maximum $-\overline{u'v'}$ in the downwash flow and upwash flow, denoted as $-\overline{u'v'}(+)^T$ and $-\overline{u'v'}(-)^B$, respectively, where $(+)$ and $(-)$ indicate the signs of $-\overline{u'v'}$ in each shear layer. In the downwash flow, the maximum $-\overline{u'v'}$ values for case A and case B are similar in the first half of the recirculation region ($x/h \in [0, 0.75]$), but further away, the profile for case A decreases more rapidly than that of case B and the maximum difference is about 55%. In the case of the upwash flow, it is evident that the maximum $-\overline{u'v'}$ profile for case B is significantly reduced compared to case A and the effect is more dramatic within the span of the recirculation region. On the other hand, the distributions of the maximum $-\overline{u'w'}$, presented in Fig. 15(b), are independent of the approach flow condition. The magnitude of $-\overline{u'v'}$ is generally larger than $-\overline{u'w'}$, except in the upwash flow of case B where $-\overline{u'v'}(-)^B$ is significantly reduced.

The anisotropic components, $b_{12} = -\overline{u'v'}/2k$ and $b_{13} = -\overline{u'w'}/2k$ are often referred to as the Townsend structure parameter. In simple turbulent shear flows, the Townsend structure parameter has an asymptotic value of 0.15. This value corresponds to a modeling coefficient, $C_\mu = (-\overline{u'v'}/k)^2 \approx 0.09$, usually used in standard RANS-based eddy-viscosity models. Figures 15(c) and 15(d) present the streamwise distributions of b_{12} and b_{13} , respectively. Except for the profile of b_{12} in the downwash flow for case A, the b_{12} profiles exhibit plateau values that are different from

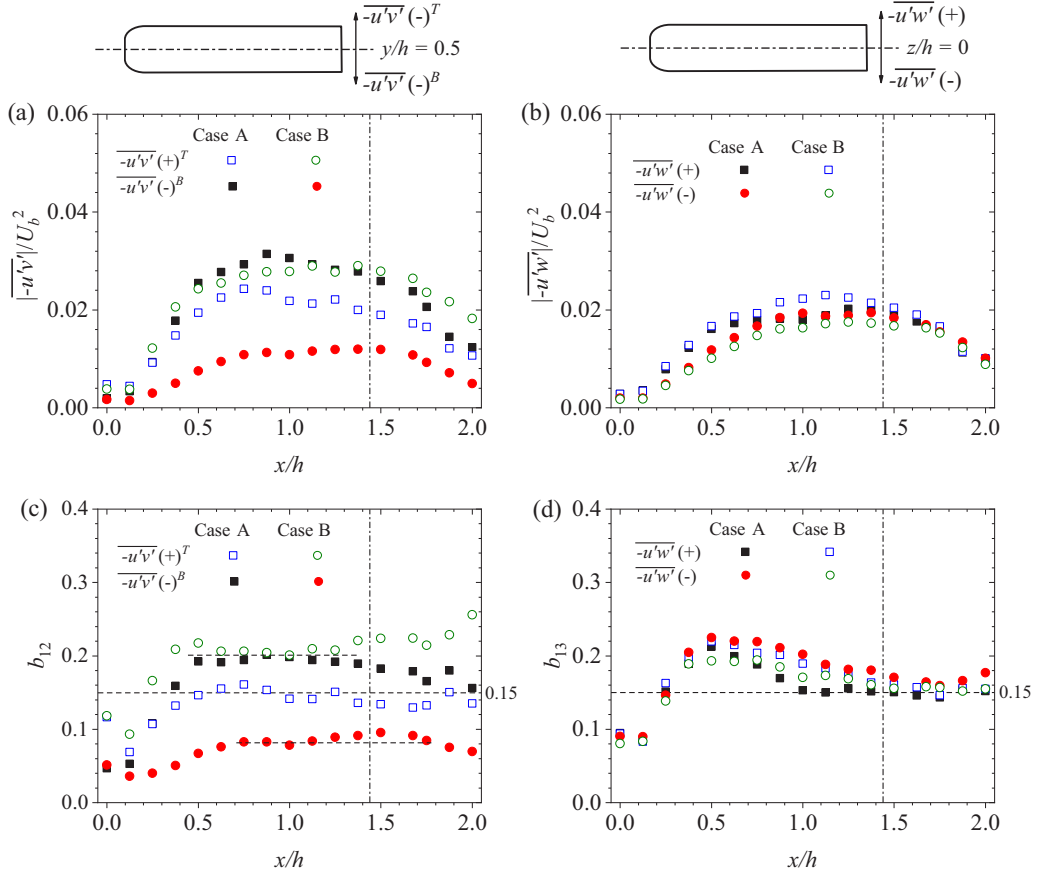


FIG. 15. Distributions of maximum Reynolds shear stresses, (a) $|\bar{u}'\bar{v}'|/U_b^2$ and (b) $|\bar{u}'\bar{w}'|/U_b^2$, and the Reynolds stress anisotropy, (c) b_{12} and (d) b_{13} , in the near wake of case A and case B. The vertical dashed line denotes the L_r/h .

0.15. In particular, the profiles of b_{12} in the downwash flow of case B and the upwash flow of case A show a plateau value of 0.20 in the region $x/h \in [0.5, 1.4]$, while the profile in the upwash flow for case B has a reduced plateau value of 0.08 in the region $x/h \in [0.8, 1.7]$. These deviations from the typical value of 0.15 demonstrate the complexity of the turbulence structure in the wall-normal plane of the near wake of the Ahmed body, especially for case B. In Fig. 15(d), the b_{13} profiles show strong deviations in the early stage of the separated shear layers, but downstream, the profiles decrease to the asymptotic value of 0.15.

D. Turbulence production

To understand the source of turbulence energy leading to the anisotropy in the Reynolds stresses in the near wake of the Ahmed body for the two approach flow conditions, the production terms of the transport equations of the Reynolds stresses were analyzed. The general equation for the production term is given as

$$P_{ij} = - \left(\overline{u_i u_k} \frac{\partial U_j}{\partial x_k} + \overline{u_j u_k} \frac{\partial U_i}{\partial x_k} \right), \quad (3)$$

where U_i are the mean velocity components and u_i are the fluctuating velocity components [60]. The production of the Reynolds normal stresses can be divided into contributions from the normal stress terms (denoted by the subscript, $-n$) and the shear stress terms (denoted by the subscript, $-s$) as follows:

$$P_{uu} = -2 \left[\underbrace{\overline{u'^2} \frac{\partial U}{\partial x}}_{P_{uu-n}} + \underbrace{\overline{u'v'} \frac{\partial U}{\partial y}}_{P_{uu-s}} + \underbrace{-\overline{u'w'} \frac{\partial U}{\partial z}}_{P_{uu-s}} \right], \quad (4)$$

$$P_{vv} = -2 \left[\underbrace{\overline{v'^2} \frac{\partial V}{\partial y}}_{P_{vv-n}} + \underbrace{\overline{u'v'} \frac{\partial V}{\partial x}}_{P_{vv-s}} + \underbrace{\overline{v'w'} \frac{\partial V}{\partial z}}_{P_{vv-s}} \right], \quad (5)$$

$$P_{ww} = -2 \left[\underbrace{\overline{w'^2} \frac{\partial W}{\partial z}}_{P_{ww-n}} + \underbrace{\overline{u'w'} \frac{\partial W}{\partial x}}_{P_{ww-s}} + \underbrace{\overline{v'w'} \frac{\partial W}{\partial y}}_{P_{ww-s}} \right], \quad (6)$$

$$P_k = (P_{uu} + P_{vv} + P_{ww})/2, \quad (7)$$

where the sum of the production terms of the Reynolds normal stresses is equivalent to the production of turbulent kinetic energy P_k .

Figure 16 shows the production terms P_{uu} , P_{vv} , P_{ww} , and P_k for each test case. In Figs. 16(a) and 16(c), P_{uu} displays asymmetric distribution in the downwash and upwash flows which is consistent with the contours of $\overline{u'^2}$ [Figs. 11(a) and 11(b)]. The contribution from the normal stress term P_{uu-n} to the net P_{uu} was found to act as an energy sink (negative production) but this energy sink was completely suppressed by the much larger energy source (positive production) from the shear stress term, P_{uu-s} . For P_{uu-s} , the term $-2\overline{u'v'}(\partial U/\partial z)$ was negligible; therefore $-2\overline{u'v'}(\partial U/\partial y)$ was the major contributor. This suggests a good approximation of the production term of $\overline{u'^2}$ in the near wake of the Ahmed body as $P_{uu} \approx -2\overline{u'v'}(\partial U/\partial y)$. By comparing Figs. 11 and 16, it is evident that the reduction in $P_{uu} \approx -2\overline{u'v'}(\partial U/\partial y)$ in the upwash flow for case B and downwash flow for case A explains the difference between $\overline{u'^2}$ for the two test cases. In Figs. 16(a) and 16(c), it is also interesting to notice a small region of production with relatively low magnitude attached to the ground for each test case. This region of production is associated with the boundary layer separation induced by APG ($\partial U/\partial x < 0$); therefore the normal stress term P_{uu-n} was found to be the energy source here.

The production terms P_{vv} [Figs. 16(b) and 16(d)] and P_{ww} [Figs. 16(e) and 16(g)] are extremely small compared to P_{uu} . This would imply that most of the energy source for $\overline{v'^2}$ and $\overline{w'^2}$ [Fig. 11] is derived from the other terms in the transport equation such as the pressure-strain and mean convection terms [59]. In terms of contributions, P_{vv-n} and P_{ww-n} were the dominant source of P_{vv} and P_{ww} , respectively, as the shear stress terms were negligibly small. Based on the above analysis, it is straightforward to observe that the turbulence production P_k [Figs. 16(f) and 16(h)] mimics the contours of P_{uu} for each test case.

E. Instantaneous vortical structures

From the unsteady simulations, the evolution of the instantaneous vortical structures can be examined to improve our understanding of the unsteady 3D wake structure around the Ahmed body and augment the above discussions on the time-averaged statistics. In the literature, several

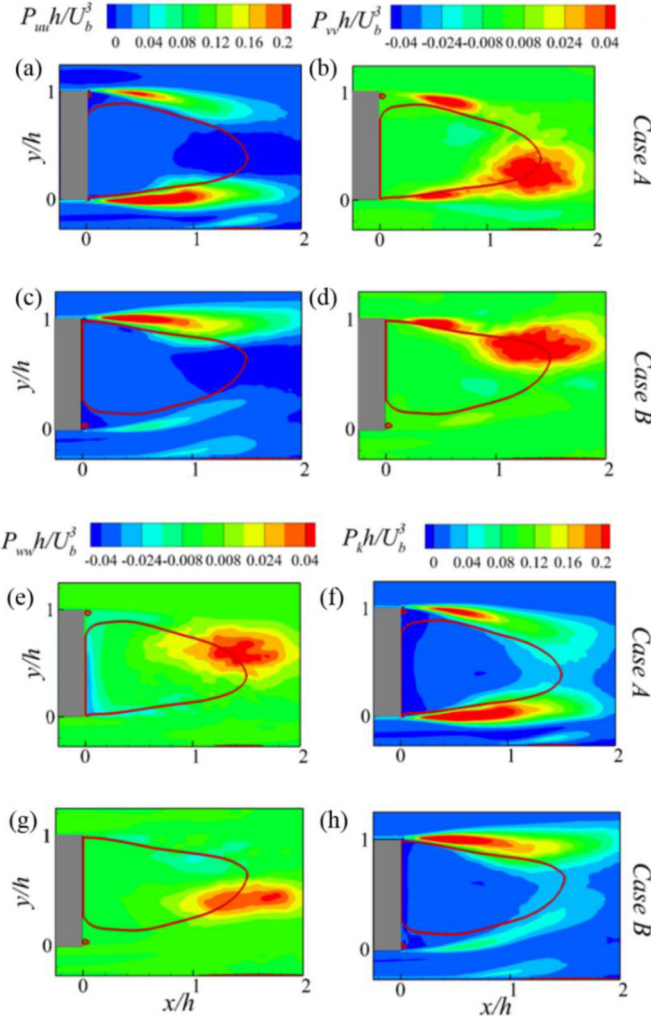


FIG. 16. Production terms of the transport equations for the Reynolds normal stresses and turbulent kinetic energy. $P_{uu}h/U_b^3$ (a), (c), $P_{vv}h/U_b^3$ (b), (d), $P_{ww}h/U_b^3$ (e), (h), and P_kh/U_b^3 (f), (h), for case A and case B, respectively. The red line represents the reverse flow region defined by the zero streamwise mean velocity contour line.

techniques have been used to identify vortical structures in turbulent shear flows. Examples include the Q criterion which is based on the complex eigenvalues of the velocity gradient tensor [63], the second invariant of the velocity gradient tensor (Δ criterion) [64], the swirling strength (λ_{ci}) [65], and the Hessian of the pressure (λ_2 criterion) [66]. In general, these techniques have been found to capture qualitatively similar vortical structures, albeit with their individual limitations [65,66]. In this study, the λ_2 criterion was used to identify the vortical structures around the Ahmed body because of earlier success in the use of the technique in bluff body flows [65,66]. The λ_2 criterion extracts the coherent vortical structures based on regions where the second largest eigenvalue (λ_2) of the tensor $S_{ik}S_{kj} + \Omega_{ik}\Omega_{kj}$ is negative [66], where $S_{ij} = (\partial U_i / \partial x_j + \partial U_j / \partial x_i)/2$ and $\Omega_{ij} = (\partial U_i / \partial x_j - \partial U_j / \partial x_i)/2$ are the symmetric and antisymmetric parts of the velocity gradient tensor $\partial U_i / \partial x_j$.

Figure 17 shows snapshots of the 3D vortical structures visualized by the λ_2 criterion and colored by the streamwise mean velocity for each test case. As shown in Figs. 17(a) and 17(b) (based on

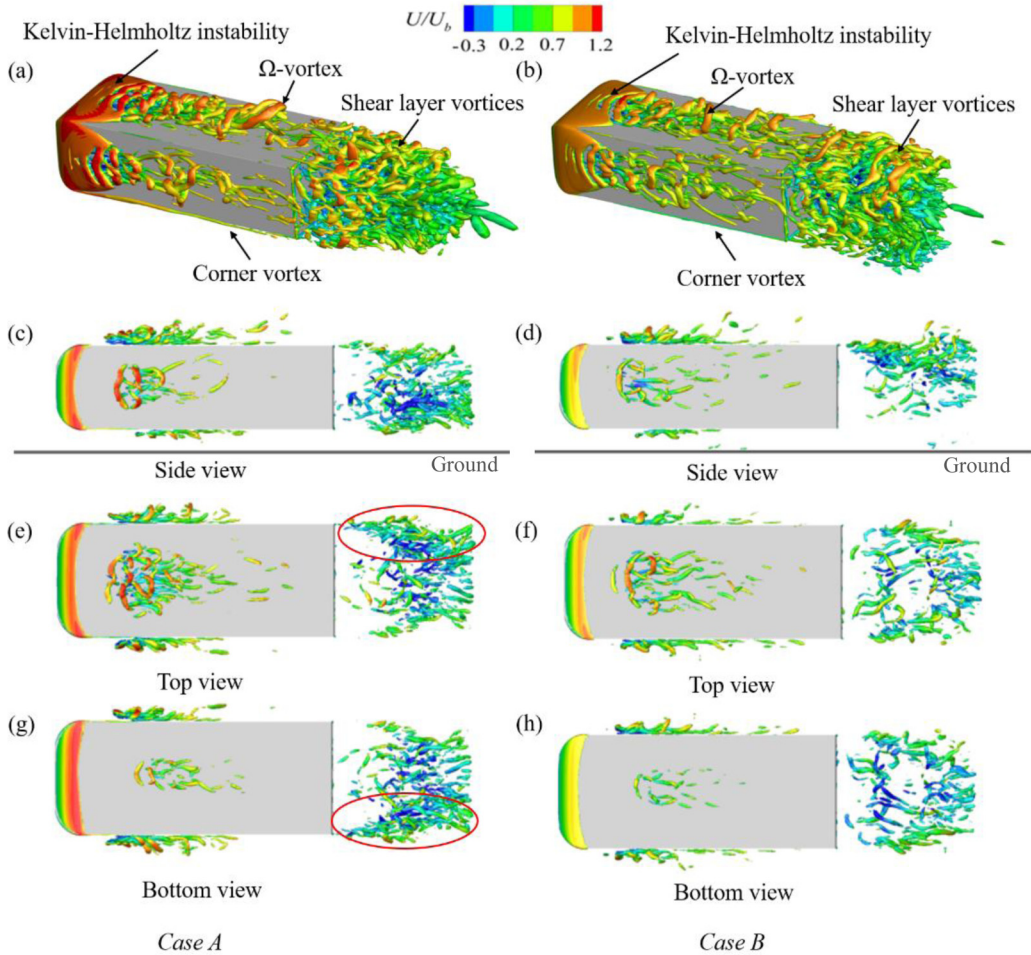


FIG. 17. Isosurfaces of λ_2 colored by instantaneous streamwise velocity: (a), (b) 3D vortical structures based on $\lambda_2 h^2/U_b^2 = -5$, and (c)–(h) planar views of the vortical structures based on $\lambda_2 h^2/U_b^2 = -50$.

$\lambda_2 h^2/U_b^2 = -5$), the vortical structures near the fore end of the body depict the separated shear layers that are influenced by the Kelvin-Helmholtz (KH) instability. After attachment, large-scale hairpinlike structures emanate from the redeveloping boundary layer on the surfaces while corner vortices are formed on the longitudinal edges of the body. The corner vortices are more pronounced on the edges of the underbody. At the rear end, these structures are shed from the body and they interact with each other to form a complex system of shear layer vortices. It is noteworthy that the various vortical structures observed in this study are consistent with results reported in previous investigations on square-back simplified vehicle models [5,12,15,34].

To visualize the differences between the two test cases, the side, top, and bottom views of the vortical structures around the body are presented in Figs. 17(c)–17(h), based on a reduced threshold value of $\lambda_2 h^2/U_b^2 = -50$ to clearly show the salient features. Figure 17(c) shows that the structures in the near wake for case A are more populated in the upwash flow than the downwash flow. In contrast, the vortical structures are clustered in the downwash flow for case B [Fig. 17(d)] but severely sparse in the upwash flow. These spatial distributions of the vortical structures are consistent with the enhanced Reynolds stresses and turbulence production in the upwash flow for case A and the downwash flow for

case B [see Figs. 11 and 16]. In the top and bottom views [Figs. 17(e)–17(h)], it is interesting to observe that the structures are more populated on the right lateral side of the wake for case A while case B shows a relatively even distribution of the structures on either side. This difference can also be seen from the isometric views of the vortical structures in Figs. 17(a) and 17(b). The asymmetry of the structures in the spanwise plane for case A signifies the occurrence of a bimodality behavior [4,12].

F. Global modes and bimodality of the wake

The complex system of shear layer vortices in the wake of the Ahmed body is associated with energetic oscillations in the wall-normal and spanwise directions, which are often referred to as global modes [8,16]. The global modes are induced by the vortex shedding behavior and the instabilities in the separated shear layers interacting with each other. As discussed in the introduction, the instabilities in the shear layer interactions may result in bimodality of the wake structure. Most previous studies identified the bimodality behavior using the temporal history of the spatial gradients of the base pressure coefficient (C_{pb}) on the rear surface of the bluff body [4,9,22,67]. However, the temporal history of the aerodynamic forces in the wall-normal (lift) and spanwise (drift) directions have also been found to produce results consistent with the spatial gradients of C_{pb} [15,29]. Here, the global modes and bimodality are explored using the lift and drift coefficients evaluated as $C_{Lf} = 2F_y/(A_f \rho U_b^2)$ and $C_{Df} = 2F_z/(A_s \rho U_b^2)$, respectively, where F_y and F_z are the instantaneous force in the wall-normal and spanwise directions, respectively, and A_f and A_s are the frontal and side areas of the body, respectively.

Figure 18 shows temporal histories of the drift and lift coefficients, and their associated probability density functions (PDFs) and joint PDFs (JPDFs) based on the total simulation time of 350 s. However, the temporal histories presented are limited to 90–210 s to highlight the interesting changes in the history of the coefficients. In Figs. 18(a)–18(d), the fluctuations in the temporal histories of the coefficients demonstrate the periodic oscillations of the global modes. For case A, two distinct peaks are present in the PDF of the drift coefficient [Fig. 18(a)], but the lift PDF [Fig. 18(c)] shows a quasi-Gaussian distribution. The double peaks of the drift PDF confirm the occurrence of bimodality of the wake in the spanwise direction, which was also observed in the spatial distribution of the instantaneous vortical structures (Fig. 17). This behavior can also be visualized from the double peaks of the JPDF contour [Fig. 18(e)]. Grandemange *et al.* [8] proposed a relational map that showed that the directional preference of the bimodality is a function of the aspect ratio and the ground clearance ratio. It is noteworthy that the map predicted spanwise bimodality for the present Ahmed body ($W/h = 1.4$ and $C/h = 0.33$), which is consistent with the current results of case A. In contrast, both the lift and drift PDFs for case B [Figs. 18(b) and 18(d)] show a quasi-Gaussian distribution and the corresponding JPDF contour [Fig. 18(f)] exhibits a single peak. These results suggest that the occurrence of bimodality is also influenced by the relative boundary layer thickness δ/H , and for $\delta/H > 1$, the thick TBL induces a strong upwash flow which suppresses the bimodality of the wake.

The temporal history of the drift coefficient for case A provides more insight into the bimodality behavior. The two asymmetric states can be distinguished by the high probability values of $C_{Df} = +0.01$ (hereafter referred to as the positive, P state) and $C_{Df} = -0.01$ (hereafter referred to as the negative, N state). It is noteworthy that when the drift coefficient is evaluated based on the frontal area (A_f), the high probability values correspond to ± 0.02 , in agreement with previous studies [12,14,15]. Figure 18(a) shows that the bimodality starts with a P state and makes the first complete switch to an N state at $t \approx 150$ s (i.e., at $C_{Df} = 0$), which corresponds to a temporal scale of $t^* = tU_\infty/h = 750$. As indicated on the plot, the duration of this wake switching event lasts for about 4.5 s ($\Delta t_{\text{switch}}^* = 22$) and it is associated with a transient symmetric state of the wake structure. At about $t \approx 200$ s ($t^* \approx 1000$), another switching event is captured where the wake changes from an N state to a P state. However, this second event is brief as the sign quickly changes back to negative and stays the same for the rest of the simulation time. This brief or incomplete switching

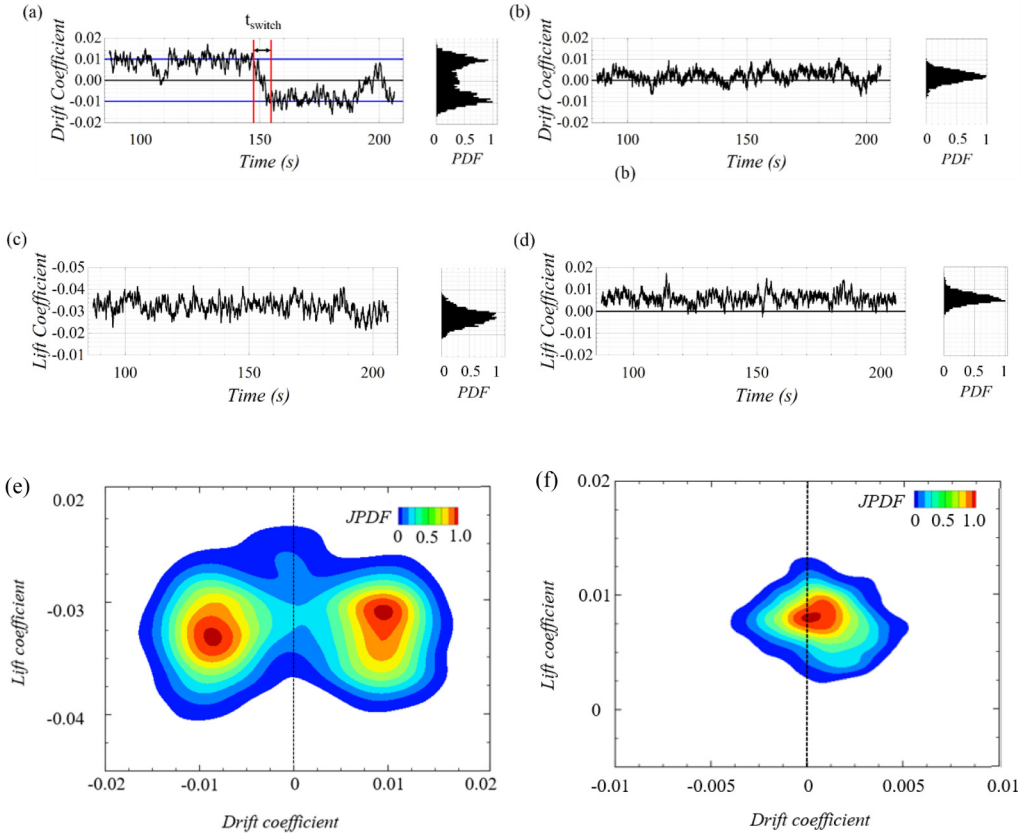


FIG. 18. Temporal histories of drift (a), (b) and lift (c), (d) coefficients along with their corresponding normalized probability density function (PDF) and joint-PDF (e), (f). The time interval of wake switching event is outlined in (a) as t_{switch} .

event has also been observed in Fan *et al.* [15] and it is attributed to the randomness of the bimodality behavior. The temporal scale for the first occurrence of the bimodality in the present study is within the values, $t^* \in [160, 1000]$, reported in the literature for square-back Ahmed bodies [3,8,15,67].

Figure 19 shows conditional averaging of the flow field based on the P and N states for case A. The flow field based on the total ensemble is included for comparison. The contours of the mean pressure coefficient on the rear surface of the body are presented in Figs. 19(a)–19(c) and the spanwise mean velocity contours at P_2 are presented in Figs. 19(d)–19(f). For the P state, the wake is skewed toward the right (positive z location) due to stronger entrainment of free stream fluid from the left side of the body. In contrast, the N state shows stronger entrainment of free stream fluid from the right side of the body which leads to the wake being skewed toward the left. Since the time duration for the two asymmetric states is comparable, the flow field based on the total ensemble exhibits a symmetric wake topography with similar entrainment from both sides of the body.

The spatiotemporal evolution of the low-pressure toroidal structure during the wake switching event is captured in the high-frequency snapshots ($\Delta t_{\text{switch}} = 147$ –153 s) presented in Fig. 20. The snapshots shown are based on a thorough inspection of animations of the instantaneous flow fields. The instantaneous C_p contours at P_2 are shown in Figs. 20(a)–20(e) and the isosurfaces of $C_p = -0.3$ are shown in Figs. 20(f)–20(j). At the onset of the switching event [Figs. 20(a) and 20(f)], the instantaneous toroidal structure in the P state experiences instabilities that leads to the tilting and stretching of the structure away from the right side of the rear end of the body. The instabilities

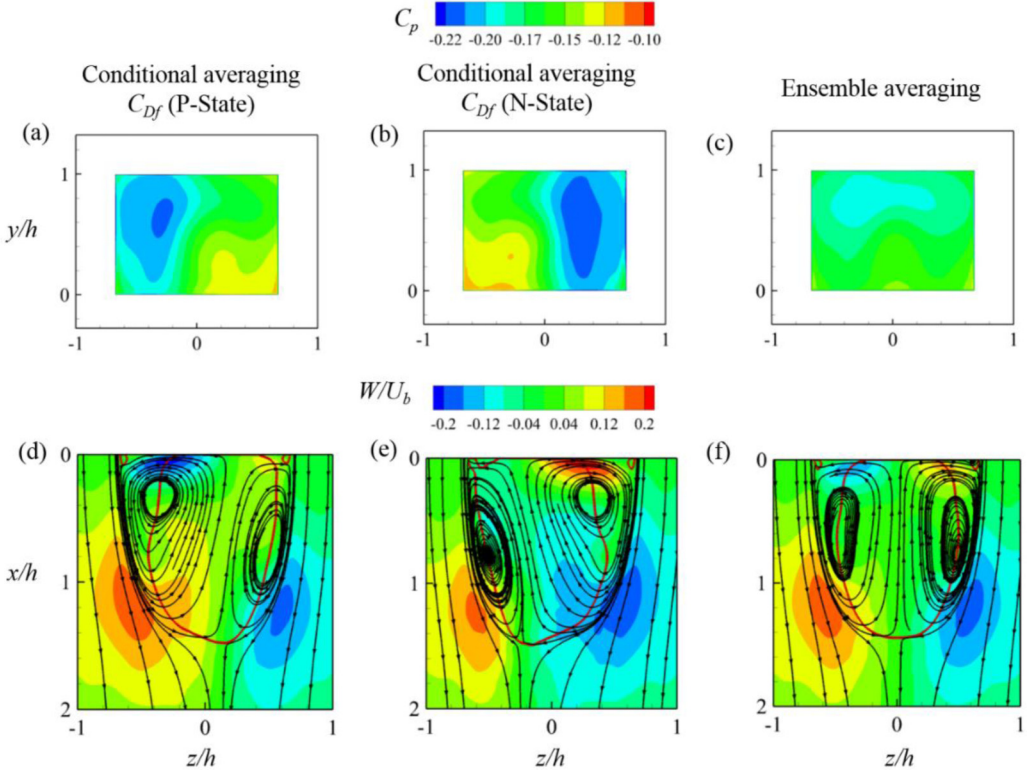


FIG. 19. Contours of C_p on rear surface (a)–(c) and spanwise mean velocity W/U_b in P_2 with streamlines superimposed (d)–(f) for case A. Conditional averaging based on the P state (a), (d) and the N state (b), (e). Total ensemble averaging based on both P and N states (c), (f). The red line represents the reverse flow region defined by the zero streamwise mean velocity contour line.

are induced by a more frequent shedding of larger hairpin vortices from the right side of the body than the left side [see Fig. 17]. The vortices combine and build up within the right part of the torus [Figs. 20(b) and 20(g)], thereby triggering the shedding of a large hairpin vortex from that part of the torus [Figs. 20(c) and 20(h)]. This large-scale hairpin vortex shedding event has also been observed in previous studies of simplified vehicle models [3,6,9,15] and it is argued to be responsible for initiating the switch between the two asymmetric states. After this event, spanwise symmetry in the low-pressure cores is restored briefly, as the vortices in the lower part of the torus build up [Figs. 20(d) and 20(i)]. Soon after, the torus becomes unstable and breaks up with the lower right part convected downstream [Figs. 20(e) and 20(j)]. Meanwhile, the shedding of larger hairpin vortices switches to the left side of the body in agreement with the new oblique orientation of the low-pressure cores (i.e., N state). It is important to note that the sequence of events captured in this study is qualitatively similar to results reported by Dalla Longa *et al.* [3] for a simplified lorry model experiencing bimodality.

To characterize the periodicity of the global modes in the wake for case A and case B, premultiplied frequency spectra of the fluctuations of the lift and drift coefficients are presented in Figs. 21(a) and 21(b), respectively. Here, the spectra of the fluctuations of the lift coefficient provide insight into the global vortex shedding timescales related to the downwash and upwash shear layers while the spectra for the drift are connected to the global vortex shedding timescales in the lateral shear layers. The spectral plots indicate that the vortical structures shed behind the body for case A are more energetic than those of case B. However, the dominant periodic global modes

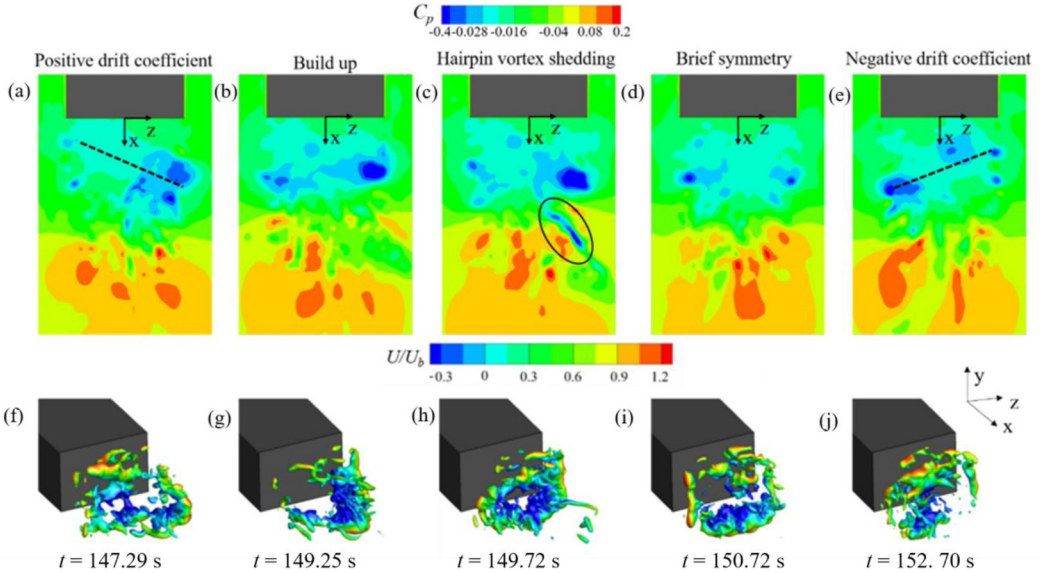


FIG. 20. Instantaneous snapshots during the interval of bimodal wake switching event indicated in Fig. 18(a) as t_{switch} . (a)–(e) Snapshots of instantaneous pressure coefficient contour in P_2 , and (f)–(j) isosurfaces of instantaneous pressure coefficient $C_p = -0.3$.

associated with the vortex shedding in the downwash and upwash shear layers [Fig. 21(a)] have a distinct Strouhal number of $\text{St} = fh/U_\infty = 0.15$, which is similar for both test cases. This Strouhal number agree well with the values, $\text{St} = fh/U_\infty = 0.13\text{--}0.19$, reported in previous investigations on the wall-normal vortex shedding timescales using spectral analysis of the velocity fluctuations at selected probe locations behind the Ahmed body [8,12,16,67]. In the lateral shear layers [Fig. 21(b)], the Strouhal number for the dominant periodic mode reduces to $\text{St} = 0.13$ and 0.10 for case A and case B, respectively. The reduction in Strouhal number in the lateral shear layers is also observed in previous studies with typical values reported as $\text{St} \approx 0.13$ [8,16,67]. However, when the Strouhal number for the lateral shear layers is defined based on the width of the body, the magnitudes of $\text{St}_W = fW/U_\infty = 0.18$ and 0.14 for case A and case B, respectively, are consistent with values reported for the downwash and upwash shear layers. In Fig. 21(b), it is also interesting to notice that the secondary periodic mode for case A exhibit a similar Strouhal number as the dominant periodic mode of case B. Nonetheless, both the lift and drift spectral plots display other periodic modes with Strouhal numbers in the range $\text{St} = 0.05\text{--}0.21$, demonstrating the large range of timescales for the vortex shedding behavior behind the square-back Ahmed body.

Figure 21(c) shows the temporal cross correlation between the lift and drift coefficients defined as

$$R_{LD} = \overline{\phi_L(t)\phi_D(t + \Delta t)} / (\phi_{L,\text{rms}}\phi_{D,\text{rms}}) \quad (8)$$

where ϕ_L and ϕ_D are the fluctuations of the lift and drift coefficients, respectively, and $\phi_{L,\text{rms}}$ and $\phi_{D,\text{rms}}$ are the root mean square value of the fluctuations, respectively. In the plot, the cross correlation on the positive timescale ($\Delta t > 0$) demonstrates the influence of the lift force on the drift (R_{LD}) while the opposite cross correlation (R_{DL}) on the negative timescale ($\Delta t < 0$) demonstrates the influence of the drift on the lift force. For case A, the cross correlation shows positive magnitudes with major peaks on either side of the timescale (i.e., $\Delta t U_\infty/h = -0.6$ and 16.4). These peaks would imply strong mutual interaction between the lift and drift forces behind the Ahmed body in a uniform flow. For the Ahmed body submerged in the thick TBL, the cross correlation in the negative section ($\Delta t < 0$) is small and tends to oscillate; however, the correlation significantly increases for

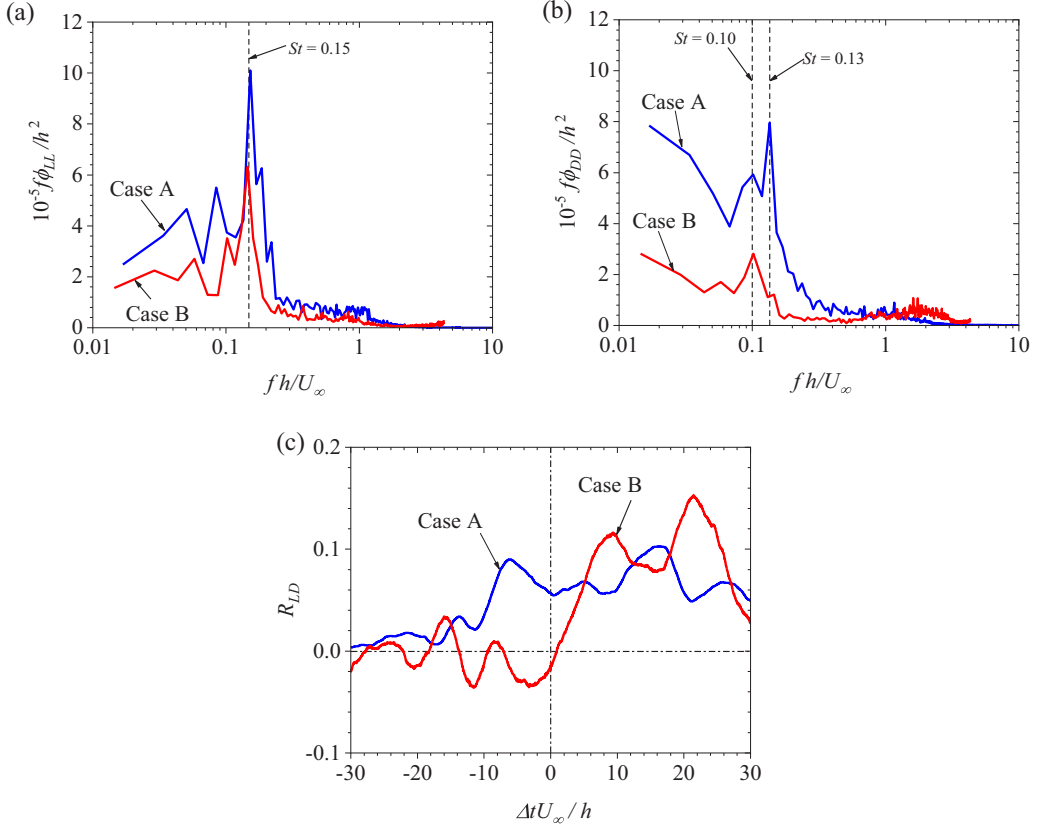


FIG. 21. Premultiplied frequency spectra profiles of the fluctuations of the (a) lift coefficient and (b) drift coefficient, and (c) temporal cross correlation between the lift and drift coefficients.

$\Delta t > 0$ with peaks (at $\Delta t U_\infty / h = 10.0$ and 21.5) that are much larger than those of case A. The enhanced cross correlation for $\Delta t > 0$ would imply that the increase in lift, perhaps due to the stronger upwash flow in case B, induces large drift force in the spanwise direction, which may suppress the occurrence of bimodality in the wake of case B.

IV. SUMMARY AND CONCLUSION

The effect of approach flow conditions on the unsteady 3D wake characteristics of an Ahmed body was investigated numerically using an IDDES hybrid RANS-LES model. Two test conditions were examined: (i) an Ahmed body encountering a uniform approach flow or thin TBL, $\delta/H = 0.09$, where H is the total height of the body from the ground (denoted as case A), and (ii) an Ahmed body fully immersed in a thick TBL ($\delta > H$), $\delta/H = 1.75$ (denoted as case B). For both cases, the Reynolds number based on the bulk velocity and body height was kept constant at $Re_b = 1.4 \times 10^4$. It is noteworthy that the flow configuration similar to case A has been examined by many previous studies, but case B has rarely been investigated.

For case B, the results showed that the elevated turbulence level and reduced mean velocity in the approach flow decreased the length of the recirculation region on the underbody by 33%, and suppressed the acceleration of the flow over the top fore end of the body when compared to case A. In the near-wake region, the length of the recirculation region ($L_r/h = 1.44$) was independent of the approach flow condition; however, the topography of the mean flow exhibits significant differences

between the two test cases. For case A, the wake is dominated by a downwash flow from the top surface, which is augmented by entrainment from the lateral sides that are intense near the top corners of the body. In contrast, the upwash jetlike flow from the underbody is dominant in the wake of case B and augmented by much stronger lateral entrainment near the bottom corners of the body. As a result, the toroidal structure formed behind the Ahmed body for case B showed significant modification from that of case A, especially on the upper and lower parts of the structure. The main difference between the wake structure of the two cases is attributed to the ground clearance momentum deficiency induced by the thick approach TBL of case B. The growth of the separated shear layers was evaluated using the vorticity thickness, which showed that the upwash shear layer for case B grows more rapidly after the recirculation region, due to a rapid diminishing of mean shear $\partial U / \partial y$ in the upwash flow. The Reynolds normal stresses ($\bar{u'^2}$, $\bar{v'^2}$, and $\bar{w'^2}$) and their corresponding production terms showed that turbulence production is more intense in the upwash shear layer of case A and the downwash shear layer of case B. This observation was mainly due to elevated mean shear ($\partial U / \partial y$) and Reynolds shear stress ($-\bar{u'v'}$) in the respective shear layer of each test case. The turbulence field also exhibited strong anisotropy in the near wake of both cases, where $\bar{u'^2} \gg \bar{v'^2}$ and $\bar{w'^2} \approx \bar{v'^2}$; however, the anisotropy tends to be more severe in case B than case A.

Periodic global modes and the occurrence of bimodality of the wake were investigated for both test cases using isosurfaces of the 3D vortical structures based on the λ_2 criterion and temporal histories of the lift and drift coefficients. Similar to previous studies, the instantaneous wake structure of case A exhibited bimodality in the spanwise direction and the timescale for the first wake switching event was $t^* = tU_\infty/h \approx 750$. However, no evidence of the bimodality behavior was found in both the wall-normal and spanwise directions of the wake structure for case B. These results suggest that the submergence of the Ahmed body in the thick TBL ($\delta > H$) induces a strong upwash flow which suppresses the mechanism responsible for the bimodality of the wake. The spectra of the lift and drift coefficients showed that the global modes associated with vortex shedding from the top and bottom rear edges have a Strouhal number $St = fh/U_\infty = 0.15$ for both test cases, but the vortex shedding from the lateral rear edges has a reduced Strouhal number of $St = 0.13$ and 0.10 for case A and case B, respectively.

ACKNOWLEDGMENTS

The authors are grateful to the Natural Sciences and Engineering Research Council of Canada (NSERC) for their financial support through a NSERC Postdoctoral Fellowship for E.E.E. and NSERC Discovery Grants for V.R. and R.B.

- [1] J. Patten, B. McAuliffe, W. Mayda, and B. Tanguay, Review of aerodynamic drag reduction devices for heavy trucks and buses, National Research Council of Canada, NRC Technical Report No. CSTT-HVC-TR-205, 2012.
- [2] S. R. Ahmed, G. Ramm, and G. Faltin, Some salient features of the time-averaged ground vehicle wake, *SAE Trans.* **473**, 840300 (1984).
- [3] L. Dalla Longa, O. Evstafyeva, and A. S. Morgans, Simulations of the bi-modal wake past three-dimensional blunt bluff bodies, *J. Fluid Mech.* **866**, 791 (2019).
- [4] M. Grandemange, M. Gohlke, and O. Cadot, Turbulent wake past a three-dimensional blunt body. Part 1. Global modes and bi-stability, *J. Fluid Mech.* **722**, 51 (2013).
- [5] D. McArthur, D. Burton, M. Thompson, and J. Sheridan, On the near wake of a simplified heavy vehicle, *J. Fluids Struct.* **66**, 293 (2016).
- [6] G. Pavia, M. A. Passmore, M. Varney, and G. Hodgson, Salient three-dimensional features of the turbulent wake of a simplified square-back vehicle, *J. Fluid Mech.* **888**, A33 (2020).

- [7] R. P. Littlewood and M. A. Passmore, Aerodynamic drag reduction of a simplified squareback vehicle using steady blowing, *Exp. Fluids* **53**, 519 (2012).
- [8] M. Grandemange, M. Gohlke, and O. Cadot, Bi-stability in the turbulent wake past parallelepiped bodies with various aspect ratios and wall effects, *Phys. Fluids* **25**, 095103 (2013).
- [9] A. Evrard, O. Cadot, V. Herbert, D. Ricot, R. Vigneron, and J. Délery, Fluid force and symmetry breaking modes of a 3D bluff body with a base cavity, *J. Fluid Struct.* **61**, 99 (2016).
- [10] Y. Haffner, J. Borée, A. Spohn, and T. Castelain, Mechanics of bluff body drag reduction during transient near-wake reversals, *J. Fluid Mech.* **894**, A14 (2020).
- [11] D. Barros, J. Borée, O. Cadot, A. Spohn, and B. R. Noack, Forcing symmetry exchanges and flow reversals in turbulent wakes, *J. Fluid Mech.* **829**, 1 (2017).
- [12] J. M. Lucas, O. Cadot, V. Herbert, S. Parpaille, and J. Délery, A numerical investigation of the asymmetric wake mode of a squareback Ahmed body—effect of a base cavity, *J. Fluid Mech.* **831**, 675 (2017).
- [13] R. Rodriguez, F. Murzyn, A. Mehel, and F. Larrarte, Dispersion of ultrafine particles in the wake of car models: A wind tunnel study, *J. Wind Eng. Ind. Aerodyn.* **198**, 104109 (2020).
- [14] G. Bonnivion and O. Cadot, Unstable wake dynamics of rectangular flat-backed bluff bodies with inclination and ground proximity, *J. Fluid Mech.* **854**, 196 (2018).
- [15] Y. Fan, C. Xia, S. Chu, Z. Yang, and O. Cadot, Experimental and numerical analysis of the bi-stable turbulent wake of a rectangular flat-backed bluff body, *Phys. Fluids* **32**, 105111 (2020).
- [16] B. Plumejeau, L. Keirsbulck, S. Delprat, M. Lippert, and W. Abassi, Behavior of the square-back Ahmed body global modes at low ground clearance, *Phys. Rev. Fluids* **5**, 084701 (2020).
- [17] B. Podvin, S. Pellerin, Y. Fraigneau, A. Evrard, and O. Cadot, Proper orthogonal decomposition analysis and modelling of the wake deviation behind a squareback Ahmed body, *Phys. Rev. Fluids* **5**, 064612 (2020).
- [18] E. Essel, S. Das, and R. Balachandar, Effects of rear angle on the turbulent wake flow between two in-line Ahmed bodies, *Atmosphere (Basel)* **11**, 328 (2020).
- [19] S. Krajnović and L. Davidson, Exploring the flow around a simplified bus with large eddy simulation and topological tools, in *The Aerodynamics of Heavy Vehicles: Trucks, Buses, and Trains* (Springer, Berlin, 2004), pp. 49–64.
- [20] A. Gulyás, Á. Bodor, T. Regert, and I. M. Jánosi, PIV measurement of the flow past a generic car body with wheels at LES applicable Reynolds number, *Int. J. Heat Fluid Flow* **43**, 220 (2013).
- [21] B. B. Herry, L. Keirsbulck, L. Labraga, and J. B. Paquet, Flow bistability downstream of three-dimensional double backward facing steps at zero-degree sideslip, *J. Fluids Eng.* **133**, 054501 (2011).
- [22] R. Li, D. Barros, J. Borée, O. Cadot, B. R. Noack, and L. Cordier, Feedback control of bimodal wake dynamics, *Exp. Fluids* **57**, 158 (2016).
- [23] D. Barros, J. Borée, B. R. Noack, A. Spohn, and T. Ruiz, Bluff body drag manipulation using pulsed jets and Coanda effect, *J. Fluid Mech.* **805**, 422 (2016).
- [24] R. D. Brackston, J. M. Garcíá De La Cruz, A. Wynn, G. Rigas, and J. F. Morrison, Stochastic modelling and feedback control of bistability in a turbulent bluff body wake, *J. Fluid Mech.* **802**, 726 (2016).
- [25] V. Gentile, B. W. Van Oudheusden, F. F. J. Schrijver, and F. Scarano, The effect of angular misalignment on low-frequency axisymmetric wake instability, *J. Fluid Mech.* **813**, R3 (2017).
- [26] G. Rigas, A. R. Oxlade, A. S. Morgans, and J. F. Morrison, Low-dimensional dynamics of a turbulent axisymmetric wake, *J. Fluid Mech.* **755**, R51 (2014).
- [27] T. Castelain, M. Michard, M. Szmigiel, D. Chacaton, and D. Juvé, Identification of flow classes in the wake of a simplified truck model depending on the underbody velocity, *J. Wind Eng. Ind. Aerodyn.* **175**, 352 (2018).
- [28] Y. Haffner, T. Castelain, J. Borée, and A. Spohn, Manipulation of three-dimensional asymmetries of a turbulent wake for drag reduction, *J. Fluid Mech.* **912**, A6 (2021).
- [29] B. Plumejeau, S. Delprat, L. Keirsbulck, M. Lippert, and W. Abassi, Ultra-local model-based control of the square-back Ahmed body wake flow, *Phys. Fluids* **31**, 085103 (2019).
- [30] O. Evstafyeva, A. S. Morgans, and L. Dalla Longa, Simulation and feedback control of the Ahmed body flow exhibiting symmetry breaking behaviour, *J. Fluid Mech.* **817**, R2 (2017).

- [31] A. Rao, G. Minelli, B. Basara, and S. Krajnović, On the two flow states in the wake of a hatchback Ahmed body, *J. Wind Eng. Ind. Aerodyn.* **173**, 262 (2018).
- [32] B. Khalighi, K. Chen, and G. Laccarino, Unsteady aerodynamic flow investigation around a simplified square-back road vehicle with drag reduction devices, *J. Fluids Eng.* **134**, 061101 (2012).
- [33] E. Guilmeneau, G. B. Deng, A. Leroyer, P. Queutey, M. Visonneau, and J. Wackers, Assessment of hybrid RANS-LES formulations for flow simulation around the Ahmed body, *Comput. Fluids* **176**, 302 (2018).
- [34] R. Lienhart, V. Jesudhas, R. Balachandar, and R. Barron, CFD study of flow around Ahmed body, in *Proceedings of 4th Thermal and Fluids Engineering Conference (TFEC)* (ASTFE, Danbury, CT, 2019), pp. 2–5.
- [35] G. Nasif, R. Balachandar, and R. M. Barron, Influence of bed proximity on the three-dimensional characteristics of the wake of a sharp-edged bluff body, *Phys. Fluids* **31**, 025116 (2019).
- [36] A. Travin, M. Shur, M. M. Strelets, and P. R. Spalart, Physical and numerical upgrades in the detached-eddy simulation of complex turbulent flows, in *Advances in LES of Complex Flows* (Springer, Berlin, 2002), pp. 239–254.
- [37] M. Perić, R. Kessler, and G. Scheuerer, Comparison of finite-volume numerical methods with staggered and colocated grids, *Comput. Fluids* **16**, 389 (1988).
- [38] H. K. Versteeg and W. Malalasekera, *An Introduction to Computational Fluid Dynamics: The Finite Volume Method* (Pearson Education, London, 2007).
- [39] P. R. Spalart, W.-H. Jou, M. Strelets, and S. R. Allmaras, Comments on the feasibility of LES for wings, and on a hybrid RANS/LES approach, in *Advances in DNS/LES*, *Proceedings of the First AFOSR International Conference on DNS/LES* (Greyden Press, Columbus, OH, 1997), pp. 137–148.
- [40] M. L. Shur, P. R. Spalart, M. K. Strelets, and A. K. Travin, A hybrid RANS-LES approach with delayed-DES and wall-modelled LES capabilities, *Int. J. Heat Fluid Flow* **29**, 1638 (2008).
- [41] P. R. Spalart, S. Deck, M. L. Shur, K. D. Squires, M. K. Strelets, and A. Travin, A new version of detached-eddy simulation, resistant to ambiguous grid densities, *Theor. Comput. Fluid Dyn.* **20**, 181 (2006).
- [42] J. Ke, RANS and hybrid LES/RANS simulations of flow over a square cylinder, *Adv. Aerodyn.* **1**, 1 (2019).
- [43] F. R. Menter, Two-equation eddy-viscosity turbulence models for engineering applications, *AIAA J.* **32**, 1598 (1994).
- [44] D. C. Wilcox, Comparison of two-equation turbulence models for boundary layers with pressure gradient, *AIAA J.* **31**, 1414 (1993).
- [45] Y. Cao and T. Tamura, Large-eddy simulation study of Reynolds number effects on the flow around a wall-mounted hemisphere in a boundary layer, *Phys. Fluids* **32**, 025109 (2020).
- [46] N. Kang, Effects of approach flow conditions on the unsteady 3D wake structure of a square back Ahmed body, M.A.Sc. thesis, University of Windsor (2020).
- [47] U. Gaitonde, Quality criteria for large eddy simulation, First year transfer report, University of Manchester (2008).
- [48] E. E. Essel, A. Nematollahi, E. W. Thacher, and M. F. Tachie, Effects of upstream roughness and Reynolds number on separated and reattached turbulent flow, *J. Turbul.* **16**, 872 (2015).
- [49] M. Kiya and K. Sasaki, Free-stream turbulence effects on a separation bubble, *J. Wind Eng. Ind. Aerodyn.* **14**, 375 (1983).
- [50] M. Yaghoubi and S. Mahmoodi, Experimental study of turbulent separated and reattached flow over a finite blunt plate, *Exp. Therm. Fluid Sci.* **29**, 105 (2004).
- [51] M. Grandemange, O. Cadot, and M. Gohlke, Reflectional symmetry breaking of the separated flow over three-dimensional bluff bodies, *Phys. Rev. E* **86**, 035302(R) (2012).
- [52] N. J. Cherry, R. Hillier, and M. Latour, Unsteady measurements in a separated and reattaching flow, *J. Fluid Mech.* **144**, 13 (1984).
- [53] N. Djilali and I. S. Gartshore, Turbulent flow around a bluff rectangular plate. Part 1: Experimental investigation, *J. Fluid Eng.* **113**, 51 (1991).
- [54] X. Fang and M. F. Tachie, On the unsteady characteristics of turbulent separations over a forward-backward-facing step, *J. Fluid Mech.* **863**, 994 (2019).

- [55] S. Jovic, An experimental study of a separated/reattached flow behind a backward-facing step. $Re_h = 37,000$, Eloret Corporation Moffett Field, NASA Technical Memorandum No. 110384, 1996.
- [56] G. L. Brown and A. Roshko, On density effects and large structure in turbulent mixing layers, *J. Fluid Mech.* **64**, 775 (1974).
- [57] E. E. Essel and M. F. Tachie, Roughness effects on turbulent flow downstream of a backward facing step, *Flow, Turbul. Combust.* **94**, 125 (2015).
- [58] A. Nematollahi and M. F. Tachie, Time-resolved PIV measurement of influence of upstream roughness on separated and reattached turbulent flows over a forward-facing step, *AIP Adv.* **8**, 105110 (2018).
- [59] M. Agelinchaab and M. F. Tachie, PIV study of separated and reattached open channel flow over surface mounted blocks, *J. Fluids Eng.* **130**, 061206 (2008).
- [60] S. B. Pope, *Turbulent Flows* (Cambridge University Press, Cambridge, 2000).
- [61] P. Bradshaw and F. Wong, The reattachment and relaxation of a turbulent shear layer, *J. Fluid Mech.* **52**, 113 (1972).
- [62] R. Simpson, Turbulent boundary-layer separation, *Annu. Rev. Fluid Mech.* **21**, 205 (1989).
- [63] M. S. Chong, A. E. Perry, and B. J. Cantwell, A general classification of three-dimensional flow fields, *Phys. Fluids A* **2**, 765 (1990).
- [64] J. C. R. Hunt, A. A. Wray, and P. Moin, Eddies, streams, and convergence zones in turbulent flows, in *Proceedings of the Summer Program* (Center for Turbulence Research, 1988), pp. 193–208.
- [65] J. Zhou, R. J. Adrian, S. Balachandar, and T. M. Kendall, Mechanisms for generating coherent packets of hairpin vortices in channel flow, *J. Fluid Mech.* **387**, 353 (1999).
- [66] J. Jeong and F. Hussain, On the identification of a vortex, *J. Fluid Mech.* **285**, 69 (1995).
- [67] R. Volpe, P. Devinant, and A. Kourta, Experimental characterization of the unsteady natural wake of the full-scale square back Ahmed body: Flow bi-stability and spectral analysis, *Exp. Fluids* **56**, 99 (2015).